Interplay between crosslinking and ice nucleation controls the porous structure of freeze-dried hydrogel scaffolds

Jérôme Grenier, Hervé Duval, Pin Lv, Fabrice Barou, Camille Le Guilcher, Rachida Aid, Bertrand David, Didier Letourneur

Interplay between Crosslinking and Ice Nucleation Controls the Porous Structure of Freeze-Dried Hydrogel Scaffolds

Jérôme Grenier[a,b,c], Hervé Duval[a,*], Pin Lv[d], Fabrice Barou[e], Camille Le Guilcher[c], Rachida Aid[c], Bertrand David[b,1], Didier Letourneur[c,1]

[a]Université Paris-Saclay, CentraleSupélec, Laboratoire de Génie des Procédés et Matériaux, 91190, Gif-sur-Yvette, France.

[b]Université Paris-Saclay, CentraleSupélec, CNRS, Laboratoire de Mécanique de Paris-Saclay, 91190, Gif-sur-Yvette, France.

[c]Université de Paris, Université Sorbonne Paris Nord, INSERM 1148, LVTS, Hôpital Bichat, F-75018 Paris, France

[d]LGPM, CentraleSupélec, SFR Condorcet FR CNRS 3417, Université Paris-Saclay, Centre Européen de Biotechnologie et de Bioéconomie (CEBB), F-51110 Pomacle, France

[e]Géosciences Montpellier, UMR 5243, Université Montpellier, CNRS, Montpellier Cedex 05, 34095, France

[*] corresponding author, e-mail address: herve.duval@centralesupelec.fr

[1] These authors contributed equally to this work.

Abstract

Freeze-drying is a process of choice to texture hydrogel scaffolds with pores formed by an ice-templating mechanism. Using state-of-the-art microscopies (cryo-EBSD, µCT, CLSM), this work evidences and quantifies the effect of crosslinking and ice nucleation temperature on the porous structure of thin hydrogel scaffolds freeze-dried at a low cooling rate. We focused on a polysaccharide-based hydrogel and developed specific protocols to monitor or trigger ice

nucleation for this study. At a fixed number of intermolecular crosslinks per primary molecule ($p = 5$), the mean pore size in the dry state decreases linearly from 240 to 170 μm, when ice nucleation temperature decreases from -6°C to -18°C. When ice nucleation temperature is fixed at -10°C, the mean pore size decreases from 250 to 150 μm, as the crosslinking degree increases from $p = 3$ to $p = 7$. Scaffold infiltration ability was quantified with synthetic microspheres. The seeding efficiency was assessed with MC3T3-E1 individual cells and HepaRG™ spheroids. These data collapse into a single master curve that exhibits a sharp transition from 100% to 0%-efficiency as the entity diameter approaches the mean pore size in the dry state. Altogether, we can thus precisely tune the porosity of these 3D materials of interest for 3D cell culture and cGMP production for tissue engineering.

Keywords

Freeze-drying, Ice-templating, Nucleation, Porous scaffolds, Infiltration, Cell seeding, Polysaccharide-based hydrogels, Tissue Engineering

1. Introduction

Hydrogels are widely used to produce scaffolds for tissue engineering (Drury and Mooney, 2003; Van Vlierberghe et al., 2011; Vashist and Ahmad, 2015; Chuang et al., 2018). They constitute a highly active field of research, with promising industrial developments and clinical applications. Hydrogel morphological, mechanical, and chemical properties are tuned to provide an optimum micro-environment for cell incorporation, proliferation, and differentiation (DeVolder and Kong, 2012). The mean pore size is one of the critical parameters that condition cell attachment, viability, and migration (O'Brien et al., 2005; Loh and Choong, 2013; Campbell et al., 2017). Its optimum depends on the biological application. Pore isotropy and pore interconnectivity are other morphological parameters to be considered as well for tissue engineering applications. Porous scaffolds can be prepared by fiber bonding, salt leaching, gas foaming, emulsion templating, or 3D printing (Liu et al., 2020). Freeze-drying is another common technique to tailor the porous structure of hydrogel scaffolds (Qian and Zhang, 2011). The pores are formed during the freezing step by a mechanism called ice-templating (Deville et al., 2006). Freezing occurs in two stages: ice nucleation at significant supercooling, followed by ice grain growth at a temperature near the ice melting point. Ice grains reject the polymer chains in the intergranular liquid since the polymer is more soluble in liquid water than in ice. When water solidification is complete, polymer chains segregate at the ice grain boundaries and form a continuous macro-network (Pawelec et al., 2014a; Zhang, 2018; Grenier et al., 2019). After the sublimation step, pores replace ice grains. Each pore is typically formed from one to a few ice grains (Grenier et al., 2019). The length scale of the macro-network is of the order of the ice grain size, i.e., orders of magnitude greater than the mesh size of the crosslinked network. Depending on the fabrication process, the crosslinking step may precede (Tao et al., 2016) or follow freeze-drying (O'Brien et al., 2004). These two steps can also be carried out simultaneously (Autissier et al., 2010).

There are several methods to freeze-dry samples. In the quench freezing, the scaffolds are immersed in a freezing agent such as liquid nitrogen. High (uncontrolled) cooling rates can be achieved, resulting in high temperature gradients and columnar solidification. The first hydrogel scaffolds with aligned pore channels have been prepared with this protocol (Kang et al., 1999). However, this method is not practical and difficult to scale up (Zhang, 2018). In directional freeze-casting, the cold finger set-up allows controlling the temperature gradient and the freezing-front velocity (modulus and direction) within a scaffold. Resulting pores are aligned with the temperature gradient and the direction of solidification. The greater the gradient, the faster the solidification, the smaller the ice grains, and the narrower the spacing between the pore channels (Deville et al., 2006; Zhang and Cooper, 2007; Deville, 2010; Bai et al., 2015; Zhang, 2018; Shao et al., 2020).

In conventional freeze-drying, the cooling rate of a sample coincides with the setpoint cooling rate of the freeze-dryer until nucleation occurs. Then, the scaffold temperature relaxes close to the ice melting point (distinct from the current setpoint temperature) as the latent heat is released (recalescence). When the solidification is complete, the scaffold temperature decreases (from the ice melting point) and returns to the setpoint temperature of the freeze-dryer. The temperature gradient within the scaffold is not controlled during the solidification. This sketch illustrates the typical behavior of thin (millimetric) scaffolds frozen at a low to moderate cooling rate. In that case, the solidification is equiaxed, resulting in a homogeneous isotropic porous structure (Kang et al., 1999; O'Brien et al., 2004; Campbell et al., 2017). The pore size homogeneity is higher at a low cooling rate (< 1°C min^{-1} in absolute value) than at a moderate cooling rate (4°C min^{-1}) (Autissier et al., 2010). A lower final freezing temperature, i.e., the plateau temperature reached at the end of the freezing, leads to a smaller mean pore size (Chung et al., 2002; O'Brien et al., 2005). As the scaffold thickness increases, the freezing time increases as well and annealing, i.e., rearrangement and coarsening of the grain structure,

may co-occur with grain growth (K M Pawelec et al., 2014a). For thick scaffolds, i.e., greater than 10 mm in all dimensions, the mean pore size is highly correlated with the so-called equilibrium time, i.e., the time spent by the scaffold close to the melting point: the mean pore size increases with the equilibrium time (K M Pawelec et al., 2014b; K. M. Pawelec et al., 2014c). Furthermore, the pore size homogeneity between the bottom and the top of a scaffold decreases as its thickness increases (Pawelec et al., 2015). After complete solidification, the time spent in the frozen state at the plateau temperature (prior to drying) also affects the mean pore size: ice annealing and resulting grain coarsening were observed after 20h at $-30°C$ (Pawelec et al., 2015). This result reported for thick scaffolds is also expected for thin ones.

Conventional freeze-drying appears as a relevant process for the production of scaffolds with isotropic porous structures. This process is mature, and the manufacturing of large quantities at a low cost is possible. This aspect is important for the market penetration and further use in routine clinical practice (Berthiaume et al., 2011).

Although conventional freeze-drying is widespread in the food and pharmaceutical industries, only a few comprehensive studies focused on the effects of process parameters on hydrogel final porous structure. Indeed, conventional freeze-drying is primarily used to preserve a product, not to irreversibly texture. In most studies, the freeze-drying protocol is optimized to get the best reconstitution properties of the product (Koivunotko et al., 2021).

On the contrary, directional freeze-casting is primarily a technique for fabricating porous materials. The physical mechanisms and the process parameters controlling the porous structure of the final material (ceramic or polymer) have been extensively investigated (Deville et al., 2006; Scotti and Dunand, 2018) and are now well described (Zhang, 2018). However, most studies consider the freeze-casting of (ceramic) particle suspensions or polymer solutions

(as opposed to cross-linked polymers). Then, ice nucleates on the cold fingers and the morphology of the growing primary crystals defines the pore structure (Deville et al., 2006).

In a recent work (Grenier et al., 2019), we studied the texturation of a polysaccharide-based hydrogel by conventional freeze-drying. The scaffolds were thin, and the hydrogel was cross-linked before freeze-drying. We found that scaffolds freeze-dried within the same batch at the same low cooling rate ($-0.1°C\ min^{-1}$), start to freeze at very different temperatures, i.e., from $-6°C$ down to $-18°C$. Each scaffold has its own nucleation temperature. We showed that the primary nucleation of ice is heterogenous and singular (Vali, 1994). Very few nucleating sites are initially present in a scaffold, i.e., of the order of 0.1 nuclei $cm^{-3}\ °C^{-1}$. Freezing is triggered by the nucleating site with the highest activation temperature, and this temperature corresponds to the scaffold own nucleation temperature. When the solidification is complete, the scaffolds have an equiaxed fine-grained polycrystalline structure. Then, we deduced that most ice grains resulted from secondary nucleation. We advanced that the rapidly growing primary ice needles rupture due to the constraints exerted by the surrounding cross-linked network, leading to intense secondary nucleation. This phenomenon is specific to freezing cross-linked polymers or hydrogels instead of polymer solutions. If this scenario is true, a higher cross-linking degree should lead to a finer ice grain size and then to a smaller mean pore size. We first tried to verify this hypothesis without controlling the nucleation temperature, and the tests (not reported in the present paper) were not conclusive: the variability of ice nucleation temperature was hiding the effect of the cross-linking degree on the final porous structure. Indeed, the supercooling degree, i.e., the difference between the ice melting point and the ice nucleation temperature, is known to impact the structure of the frozen product and, subsequently, the porous structure of the freeze-dried product (Pawelec et al., 2014c; Zhang, 2018; Searles et al., 2001).

In the present work, we monitored the ice nucleation temperature within scaffolds to examine its effect on the porous structure at a fixed formulation and a fixed cooling rate. We also

triggered ice nucleation at given supercooling to examine the effect of the cross-linking degree on the porous structure at a fixed ice nucleation temperature.

Whereas the effects of cooling rate (O'Brien et al., 2004), final freezing temperature (O'Brien et al., 2005), scaffold thickness, mold design were investigated for conventional freeze-drying, this is the first time, to the best of our knowledge, that the effect of ice nucleation temperature was studied for freeze-dried hydrogel scaffolds. Furthermore, the effect of crosslinking on ice grain size and resulting pore size was rigorously quantified, free from the effects of stochastic variations of ice nucleation temperature. Last, the interplay between crosslinking and ice nucleation is specific to the freeze-drying of hydrogels, and this phenomenon is not met when ice-templating colloid suspensions or polymer solutions.

The present study deals with thin polysaccharide-based hydrogel scaffolds (disks of thickness < 5 mm and diameter > 10 mm) freeze-dried at a low cooling rate ($-0.1°C\ min^{-1}$) and a low drying pressure (primary drying at 0.010 mbar). We used a "minimal" formulation, consisting only of polymers and crosslinker: a blend of pullulan and dextran crosslinked in an aqueous phase with sodium trimetaphosphate (STMP) (Lavergne et al., 2012; Grenier et al., 2019). This biomaterial family is under research and industrial developments: it is relevant for tissue engineering applications (Chaouat et al., 2006; Fricain et al., 2013), its biocompatibility and its biodegradability were demonstrated (Lanouar et al., 2018), and it can promote 3D cell organization (Guerrero et al., 2013). In particular, hydrogel scaffolds were used to produce functional and viable hepatic constructs (Labour et al., 2020), hydroxyapatite/hydrogel composites were successfully applied to in vivo bone repair (Fricain et al., 2013).

We know that many properties have to be considered for the use of hydrogel scaffolds in tissue engineering. The present paper chooses to focus on the morphological and morphology-related properties. The hydrogel scaffolds were carefully characterized at each step of the fabrication

process. The crosslinking kinetics and the final crosslinking degree were determined by oscillatory rheology. The microstructure of the frozen hydrogel at the end of the freezing stage was analyzed using cryogenic electron backscatter diffraction (EBSD) at -100°C (Piazolo et al., 2008; Grenier et al., 2019). After the drying stage, a detailed 3D analysis of the pore size distribution in the dry state was performed by X-ray computed tomography. Then, the porous structure in cell culture conditions (swollen state) was investigated with Confocal Laser Scanning Microscopy (CLSM). The infiltration ability of the freeze-dried scaffolds was carefully quantified with a series of narrow-sized calibrated microspheres (Shepherd et al., 2018), and the seeding efficiency was assessed with individual MC3T3E1 osteoblast cells and HepaRG^{TM} hepatocyte spheroids.

Finally, a thorough analysis of the experimental results provides the mechanisms that link the scaffold mean pore size to the crosslinking degree and to the supercooling degree during freeze-drying. These findings will help to control and optimize the porous structure of hydrogel scaffold for 3D cell culture and future cGMP productions.

2. Materials and methods

2.1. Polysaccharide-based hydrogel scaffolds

2.1.1. Polymer solution

The polymer aqueous solution contained pullulan (225 g L^{-1}) and dextran (75 g L^{-1}) with NaCl (35 g L^{-1}). Pullulan (200 kDa) was purchased from Hayashibara, and dextran (500 kDa) from Pharmacosmos. The number average molecular weight (M_n), the polydispersity (I_p), and the gyration radius (s) of the polymers were determined by combining size exclusion chromatography with multi-angle light scattering analysis (Grenier et al., 2019). Pullulan chains were characterized by M_n = 158.8 kg mol^{-1}, Ip = 1.98, and s = 17.1 nm, dextran by M_n = 284.9 kg mol^{-1}, Ip = 1.82, and s = 16.0 nm. The number average molecular weight of the

polymer mixture was then M_n = 178.6 kg mol^{-1} and the mean gyration radius s = 16.9 nm. It should be noted that dextran was substituted at 0.17 % (w/w) by FITC-labeled dextran (TdB Consultancy) for confocal imaging.

2.1.2. Hydrogel preparation with different crosslinker feed ratios

The polymer mixture was crosslinked with sodium trimetaphosphate (STMP from Sigma-Aldrich) under alkaline conditions (NaOH) at 50°C for 20 minutes. The mold consisted of two horizontal plates spaced 1 mm apart. Four formulations were studied. They only differed in the STMP amount added to the polymer solution. In the following, each hydrogel formulation is identified by its crosslinker feed ratio (r), defined as the ratio of moles of STMP to the number of moles of polymer: r = 48, 72, 96, and 161 mol mol^{-1}. The STMP concentration in the crosslinking solution was then equal to 0.049, 0.073, 0.098, or 0.163 mol L^{-1}, respectively. The concentrations of the other components were fixed, *i.e.*, [pullulan] = 8.18 10^{-4} mol L^{-1}, [dextran] = 1.52 10^{-4} mol L^{-1}, [NaCl] = 3.46 mol L^{-1} and [NaOH] = 0.953 mol L^{-1}. The overall polymer concentration is about three times greater than the overlap concentration that is estimated at 3.4 10^{-4} mol L^{-1} (de Gennes, 1979). The overall concentration of anhydroglucose units is [AGU] = 1.07 mol L^{-1}.

After the crosslinking stage, the hydrogel layer is cut into scaffold disks (diameter of 5 mm), then neutralized by Dulbecco's Phosphate Buffered Saline (DPBS, Sigma Aldrich, 10x), and finally washed with NaCl (0.25 g L^{-1}) (Grenier et al., 2019). In the following, the basal plane of the scaffolds is denoted *XY* and the symmetry axis *Z*.

2.1.3. Polymer solution and hydrogel characterization

The dynamic viscoelastic properties of the polymer solution during the crosslinking were investigated with Discovery HR-2 (TA Instrument) rheometer. The crosslinking process was reproduced in the rheometer at 50°C for 20 minutes using a parallel-plate device (diameter = 4

cm, gap between plates = 1 mm), at a frequency of 1Hz, at a shear strain amplitude of 0.1% (linear domain), with axial force lower than 0.1 N. The number average molecular weight between crosslinks (M_c) was computed from the final storage moduli (G') assimilating G' to the static shear modulus (G) and using the rubber elastic-theory (Peppas and Merrill, 1977; Treloar, 1975). We verified that the hydrogel is highly elastic (loss tangent much lower than 1) at the end of the crosslinking stage.

Since the polymer is kept in the solvent used for crosslinking, it is in the relaxed state, and the relation between G and M_c reads:

$$\mathrm{G} = \frac{R\,T\,C_{2r}}{M_c}\left(1 - \frac{2M_c}{M_n}\right) \tag{1}$$

where R is the gas constant (J mol^{-1} K^{-1}), T is the temperature (K), and C_{2r} is the polymer concentration in the relaxed state (kg m^{-3}). Furthermore, the number of intermolecular crosslinks per primary molecule (p) is given by $p = M_n/M_c$.

Since the reaction rate at 50°C is high, the gel point was crossed very quickly and could not be studied at that temperature. Instead, gelation was investigated at 25°C. Storage modulus (G'), loss modulus (G'') and loss tangent ($\tan\delta = G''/G'$) were measured every 30 seconds using cone-plate geometry at 0.1% strain, at 4 frequencies, *i.e.*, 0.5, 1, 2, and 5 Hz. These frequencies were below the inverse of the largest relaxation time of the primary molecules, *i.e.*, their reptation time, of the order of 5×10^{-6} s. Reptation may occur since the mass of the primary molecules is greater than ten times the entanglement molecular weight, i.e., $M_e \cong 10^5$ Da in the present concentration range (Horinaka et al., 2012). Then, the gel point or gelation time ($t_{gelation}$) corresponds to the instant at which the curves $\tan\delta$ vs time intercept (Holly et al., 1988). At this instant, the storage and loss moduli follow a frequency power law with the same exponent (Chambon and Winter, 1987).

Additional characterizations were carried out after the crosslinking step, i.e., on the hydrogel kept in the solvent used for crosslinking, and after the washing step, i.e., on the hydrogel swollen in NaCl (0.25 g L^{-1}). The volume fraction of the polymer in the relaxed state (v_{2r}) and in the swollen state (v_{2s}) were determined by weighting (n = 3 scaffolds per crosslinker feed ratio). The conversion from mass fraction to volume fraction was done according to (Grenier et al., 2019). The swelling ratio (Q), defined as the ratio of v_{2r} to v_{2s}, was calculated as well. Then, the mesh size in the relaxed state (ξ_r) and in the swollen state (ξ_s) are determined from the end-to-end distance of the chains in the unperturbed state $\left(\overline{r_0^2}\right)^{\frac{1}{2}}$ (Canal and Peppas, 1989):

$$\xi_{r,s} = v_{2r,s}^{-\frac{1}{3}}\left(\overline{r_0^2}\right)^{\frac{1}{2}} \quad (2)$$

Since there is no model of end-to-end distance for chains made of both pullulan and dextran, $\left(\overline{r_0^2}\right)^{\frac{1}{2}}$ was estimated under 100% pullulan and 100% dextran assumption (Grenier et al., 2019).

The phosphorus content of the hydrogel after the washing step was determined by spectrophotometry (Infinite M200 Pro from TECAN) at 405 nm after complete dissolution of the hydrogel in 10% (v/v) HNO_3 at 105°C and addition of NH_4VO_3 and $(NH_4)_6Mo_7O_{24}$ (Lanouar et al., 2018). A series of H_3PO_4 solutions were used as standards for calibration. For each formulation, three hydrogel preparations were carried out. For each preparation, the analysis protocol was performed in triplicate. The standard deviation of the replicates from the same preparation was less than 7%. The phosphorus content of the hydrogel (c_P) is given as the ratio of moles of grafted phosphorus to the number of moles of polymer in the feed.

2.2. Scaffold texturation by freeze-drying

The hydrogel scaffolds were successively swollen in NaCl (0.25g L^{-1}), drained to remove the solvent excess, arranged in a single layer on the bottom of Petri dishes (scaffold basal plane parallel to the bottom), and placed on freeze-dryer trays (MUT 004, Cryotec®). The freeze-

drying protocol consisted of four stages: cooling under atmospheric pressure at a constant rate of -0.1°C min^{-1} from 5°C to – 20 ˚C, holding at -20°C during 90 min, primary drying at 0.010 mbar and -5°C for 8 h and secondary drying at 30°C for 1 h (Le Visage et al., 2015; Grenier et al., 2019). Two parameters may differentiate the different batches: the separation distance between scaffolds within a Petri dish and the way nucleation occurred. Scaffolds were either contiguous, i.e., contacts between scaffolds, or spaced, i.e., no contact between scaffolds (**Fig. S4** in Supplementary materials). Ice nucleation occurred either spontaneously during the cooling step, or was triggered by a brief pressure variation within the freeze-dryer chamber. The nucleation temperature was assimilated to the plate temperature when the nucleation occurred, as evidenced by a rapid change in scaffold opacity (Grenier et al., 2019). The supercooling degree defined as the difference between the water freezing point and the nucleation temperature is denoted ΔT.

A batch of scaffolds with $r = 96$ mol mol^{-1} was freeze-dried in spaced configuration. Nucleation temperature was monitored for each scaffold.

Batches of scaffolds with r from 48 to 161 mol mol^{-1} were freeze-dried with pressure variation protocol: the nucleation temperature was set at -10 ± 0.2°C.

2.2.1. Analysis of frozen scaffolds using cryogenic electron backscatter diffraction

Some batches were intentionally interrupted before the primary drying step. The frozen scaffolds were then collected from the freeze-drier and stored at -80°C. The microstructure of the frozen scaffolds was analyzed in cold conditions using the CamScan Crystal Probe X500FE SEM-EBSD (CNRS UMR 5243, University of Montpellier), equipped with C1001 GATAN gaseous nitrogen cold stage modulus. Scaffolds were maintained at -95 ± 5°C with 1 Pa vacuum. Electron Backscattering Diffraction (EBSD) was performed with 20 µm step size (Grenier et al., 2019). Aztec software package from Oxford Instruments HKL was used to

index EBSD pattern. Indexation of ice crystal from hexagonal space group 186 with a = 4.51 Å and c = 7.34 Å was successful over more than 90 % of the surface with less than 0.5° angular resolution. Channel5 software package was used to process EBSD patterns into Inverse Pole Figure (IPF) orientation map. Ice grains were defined as continuous domains with less than 10° crystallographic misorientation. The ice grain size was computed as the square root of the grain area.

2.2.2. Analysis of freeze-dried scaffolds using X-ray tomography

The porous structure of the freeze-dried scaffolds was characterized with a voxel size of (6 µm)^3 using an X-ray nanotomograph EasyTom XL 150/160 from RX (ultimate resolution of 0.4 µm). We preferred this technique to the "gold standard" SEM 2D image analysis because X-ray tomography directly assess 3D structure. We emphasize that the whole scaffold volume was acquired and analyzed, the resolution was adjusted to accurately capture the pore walls. Acquisition parameters and reconstruction procedure have been previously described (Grenier et al., 2019). Pores were isolated in 3D using Avizo software (Thermo Scientific) after thresholding, hole filling, object separation (using watershed algorithm), and labelling. The pore size was defined as the cubic root of the 3D pore volume. We also characterized the pore morphology and determined the Feret shape (defined as d/D where d is the minimum Feret diameter and D is the maximum Feret diameter in the orthogonal direction) of the pores and their inclination to Z-direction. Three scaffolds were analyzed per parameter setting (crosslinker feed ratio and nucleation temperature).

2.2.3. Pore size analysis of swollen scaffolds using CLSM

CLSM (ZEISS LSM700) was used to characterize the porous structure of FITC-labeled swollen scaffolds. After freeze-drying, scaffolds were allowed to swell overnight in DPBS. XY views (parallel to the basal plane of the swollen scaffolds) were acquired and processed with

ImageJ (Schneider et al., 2012). The pore size was estimated as the square root of the measured area on the XY plane.

2.3. Infiltration tests with narrow-sized calibrated microspheres

Suspensions of narrow-sized calibrated microspheres were used to quantify the scaffold infiltration ability (Shepherd et al., 2018) over a wide range of diameters, *i.e.*, from mammalian cell size to large spheroid size. Fluorescent red polyethylene microspheres UVPMS-BR from Cospheric were dispersed in DPBS (5‰ (v/v) of microspheres) with the addition of surfactant (1% (w/v) of Tween 80®). The microsphere diameter (d_s) was 3 ± 1 µm, 15 ± 5 µm, 58 ± 5 µm, 115 ± 10 µm, 275 ± 25 µm, 463 ± 38 µm, and 655 ± 55 µm. 20 µL of microsphere suspension was deposited on top of the freeze-dried scaffolds. This method corresponds to a static seeding (Palmroth et al., 2020). Complete swelling of the scaffolds was achieved by further addition of DPBS. DPBS was added in excess to wash the non-entered microspheres.

The infiltration efficiency (E) is defined as the ratio of the number of microspheres entrapped in the scaffold to the total number of microspheres deposited on the top of the scaffold. The number of trapped microspheres was obtained by counting the microspheres remaining in the supernatant. Seeded scaffolds were also analyzed by CLSM (ZEISS LSM 700). XZ views (orthogonal to the basal plane) of the scaffolds were acquired over 250-µm depth in 43 confocal slices of 2.5 µm pixel size. The red channel corresponds to the red microspheres signal and the green channel to the FITC-hydrogel. Images were processed using ImageJ to detect the microspheres and the pores. The pore size was computed as the square root of the pore area in the current XZ cross-section. Since a microsphere cannot enter pores smaller than its diameter, microspheres tend to segregate in larger pores. In order to quantify this phenomenon, we defined the exclusion coefficient F as the ratio of the mean size of the occupied pores to the overall mean pore size. Infiltration tests were performed in triplicate.

2.4. Cell seeding of freeze-dried scaffolds

MC3T3E1 cells (ATCC) with a diameter of 18 ± 1 µm in suspension (Klembt Andersen et al., 2005) were cultivated under standard cell culture conditions (α-MEM medium with nucleosides without ascorbic acid (GIBCO), supplemented with 10% FBS (South America, Dutscher)). The cells were trypsinized with Trypsin/EDTA (PAN-Biotech) and labeled with PKH-26 red dye according to manufacturer instructions (Phanos Technologies). 20 µL of cell suspension with 100,000 individual cells were seeded on top of the freeze-dried porous hydrogel scaffolds. Complete swelling of the scaffolds was achieved by the addition of cell culture medium. 24 hours post-seeding, the seeded scaffolds were rinsed twice with DPBS and cells were fixed in 4% (v/v) paraformaldehyde during 24 hours.

HepaRG™ cells (HPR101 - Undifferentiated HepaRG™) were amplified two weeks under standard cell culture conditions in proliferating medium (MIL700C - Basal hepatic cell medium with ADD710C - HepaRG™ Growth Medium - Supplemented with antibiotics according to manufacturer instructions) (Gripon et al., 2002). Then, wells from 96-well Nunclon™ Sphera™ microplates were seeded either with 1,500 or with 3,000 HepaRG™ cells to form spheroids. The expected spheroid diameter was 150 ± 50 µm or 250 ± 60 µm, respectively (Bell et al., 2016). After 7 days, 32 spheroids were harvested in 20 µL culture medium suspension and seeded on top of the freeze-dried scaffolds. The addition of cell culture medium achieved complete swelling of the scaffolds. 2 hours post-seeding, the seeded scaffolds were rinsed twice with DPBS and spheroids were fixed in 4% (v/v) paraformaldehyde during 24 hours at 4°C. Then, cells were permeabilized by 0.1% (v/v) Triton X from *Sigma Aldrich*. Nuclei were stained with 1/5000 (v/v) DAPI from *Thermo Fischer*, and actin cytoskeletons were stained with 1/200 (v/v) TRITC-Phalloidin from *Sigma Aldrich* for 2 hours at room temperature.

Finally, the seeded scaffolds (with MC3T3-E1 or HepaRG^{TM} spheroids) were equilibrated with DPBS. XY views (parallel to the scaffold basal plane) were acquired by CLSM (ZEISS LSM 700) over 400-µm depth in 23 slices with 1.25 µm pixel size.

Experiments were performed on n = 6 independent samples per group of MC3T3-E1 or HepaRGTM.

2.5. Data analysis

The values are given as mean (points) ± standard deviation (bars) calculated over at least 3 independent samples. It happens that the error bars are smaller than the point size (**Fig 2**). The distributions are represented either entirely by their frequency curves or by box and whisker plots with the ends of the box standing for the first and third quartiles, the middle horizontal line of the box being the median, and the ends of the whiskers representing the 10th and 90th percentile (**Fig. 4 D**).

3. Results

3.1. Crosslinking of the polysaccharide mixture

Crosslinking at 50°C was followed, for the four crosslinker feed ratios, by dynamic shear rheology at 1 Hz using a plate-plate geometry with 1 mm gap, similarly to the mold used for the scaffolds preparation. We observed that the storage modulus increased rapidly during the first minutes of the process (**Fig. 1**), consistently with the conclusions of the gel point study at 25°C (see **Fig. S1** and related comments in Supplementary materials). *G'* reached its maximal value (G'_{max}) after 6 to 11 minutes and then slightly decreased to its final value (G'_{final}) at 20 min (**Fig. 1**). G'_{max} and the corresponding time t_{max} are well correlated with the crosslinker feed ratio (see **Fig. S2** in Supplementary materials). In the present study's parameter range, G'_{max} and t_{max} increase linearly with r (R^2 = 0.9901 and R^2 = 0.9905, respectively). On the

other hand, the final value of the storage modulus is better correlated with the phosphorus content (c_P) of the resulting hydrogel (**Fig. 2B**): G'_{final} increases linearly with c_P ($R^2 = 0.989$).

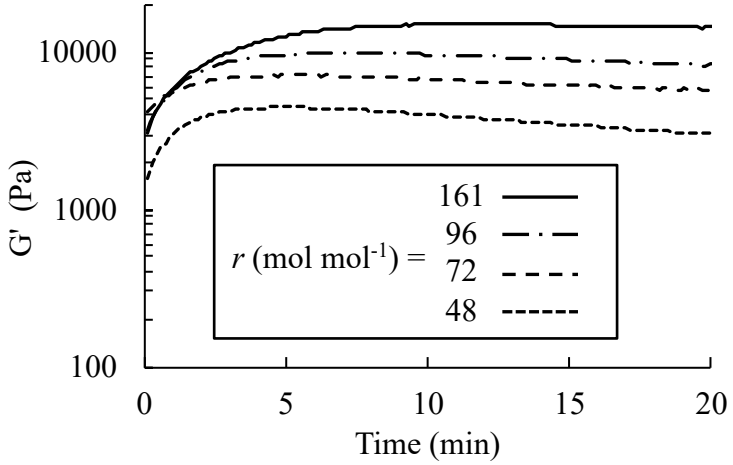

Fig. 1. Variations of the storage modulus at 1 Hz during crosslinking at 50°C. Crosslinker feed ratio r = 48 mol mol^{-1} (dotted line), 72 mol mol^{-1} (dashed line), 96 mol mol^{-1} (dash-dotted line), 161 mol mol^{-1} (continuous line).

The phosphorus content of the hydrogel (c_P) was measured by spectrophotometry. We observed that c_P is proportional ($R^2 = 0.994$) to the crosslinker feed ratio up to r = 100 mol mol^{-1}, i.e. [STMP] = 0.1 mol L^{-1} (**Fig. 2A**). Beyond r = 100 mol mol^{-1}, c_P increases more slowly with r. Because the [NaOH]/[AGU] ratio is large in the present experiments, we may assume that the grafted tripolyphosphate (the main reaction intermediate) is almost entirely converted into phosphate mono- and diesters (Lack et al., 2007, 2004). Then, the linear regression slope gives the yield of the phosphate grafting, equal to 49 ± 1 % (mol mol^{-1}). For r = 161 mol mol^{-1}, i.e. [STMP] = 0.163 mol L^{-1}, the yield is lower, i.e. 40 ± 1 % (mol mol^{-1}). These results are consistent with the trend reported in the literature (the grafting yield decreases from 40% when [STMP] ≤ 0.1 mol L^{-1} to 26% when [STMP] = 0.21 mol L^{-1}) (Dulong et al., 2011). A

theoretical estimate of the minimal crosslinker feed ratio to form a gel (percolation threshold) can be deduced by extrapolating our data, i.e., r_{min} = 28.3 mol mol^{-1} (triangle in **Fig. 2B-D**).

Using Eq. 1 from the rubber elastic-theory, the number of intermolecular crosslinks per primary molecule in the final hydrogel (p) was deduced from the final value of the storage modulus (G'_{final}) using (Peppas and Merrill, 1977; Treloar, 1975). We found that p increased linearly (R^2 = 0.984) with the phosphorus content (**Fig. 2C**). Since each intermolecular crosslink is shared by two primary molecules, the fraction of efficient links, i.e., the ratio of phosphorus implied in intermolecular crosslinks to the total incorporated phosphorus is equal to half of the linear regression slope: 5.4 ± 0.2 % (mol mol^{-1}). Interestingly, this value is one order of magnitude lower than the efficient fractions reported in the literature (between about 40% and 80%) (Dulong et al., 2011). We presently calculated about 17 monoester bonds for one intermolecular diester bond per chain (intramolecular diester bonds were neglected). For the extrapolated feed ratio r_{min} = 28.3 mol mol^{-1}, calculating the number of intermolecular crosslinks per primary molecule gave p = 1.5 to be compared with the theoretical percolation threshold p = 1 (Flory, 1953). For the crosslinker feed ratio r = 48 mol mol^{-1} (phosphorus content of 24 mol mol^{-1}), p is equal to 2.5, whereas $p > 2$ corresponds to the case of a "true" polymer network.

The mesh size in the relaxed state (ξ_r) and in the swollen state (ξ_s) was computed from the end-to-end distance of the chains in the unperturbed state (Canal and Peppas, 1989). As the crosslinker feed ratio increases, more phosphodiester bonds are created until 6 per polymer chain for r = 161 mol mol^{-1} (**Fig. 2C**), and consequently, the storage modulus *G'* increases (**Fig. 2B**). At the same time, ξ_r decreases from 38 nm to 26 nm when r increases from 48 to 161 mol mol^{-1} (**Fig. 2D**).

The swelling ratio of the hydrogel in NaCl (0.25 g L^{-1}) decreases with the phosphorus content (and correlatively with the crosslinker feed ratio) from 14 ± 0.6 m^3 m^{-3} to 7 ± 0.6 m^3 m^{-3} (**Fig. 2E**). Consistently, the mesh size in the swollen state (ξ_s) is larger than in the relaxed state and decreases with the phosphorus content from 91 nm to 34 nm, computed under 100% pullulan assumption (**Fig. 2F**). The swelling is also strongly affected by the ionic strength of the solvent: the swelling ratio in Dulbecco's Phosphate Buffered Saline (DPBS) is one order of magnitude lower than in NaCl (0.25 g L^{-1}). It decreases with the phosphorus content from 4.32 ± 0.24 m^3 m^{-3} to 2.56 ± 0.13 m^3 m^{-3} (see **Fig. S3** in Supplementary materials).

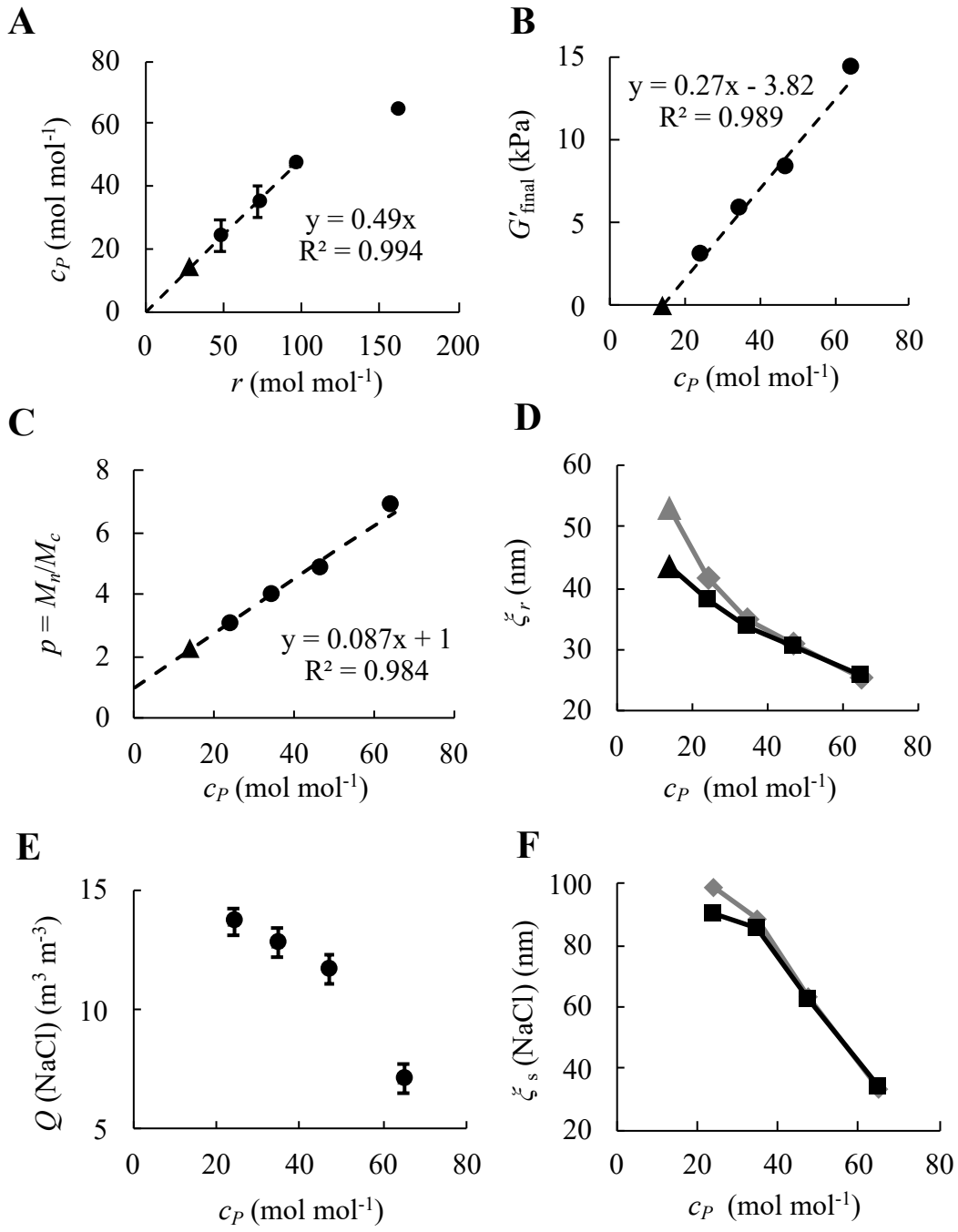

Fig. 2. Characterization of the STMP crosslinked pullulan-dextran mixture. **A**: Phosphorus content c_P (dots) as a function of the crosslinker feed ratio. The triangle corresponds to the phosphorus content extrapolated at zero final storage modulus, i.e., c_P = 14.15 mol mol^{-1} with respective crosslinker feed ratio r = 28.3 mol mol^{-1}. **B**: Final value of the storage modulus G'_{final} (dots) as a function of the phosphorus content. The triangle corresponds to the

extrapolated point G'_{final} = 0 with respective phosphorus content of 14.15 mol mol^{-1}. **C**: Average number p of intermolecular crosslinks per primary molecule (dots) as a function of the phosphorus content. The triangle corresponds to the number of intermolecular crosslinks per primary molecule (p = 2.2) extrapolated at G'_{final} = 0. **D**: Mesh size ξ_r in the relaxed state, computed under 100% dextran (gray diamonds) and 100% pullulan assumption (black squares) as a function of the phosphorus content. **E**: Swelling ratio Q(NaCl) (dots) of the hydrogel in NaCl (0.250 $g.L^{-1}$) as a function of the phosphorus content. **F**: Mesh size ξ_s in the swollen state in NaCl (0.250 g L^{-1}) computed under 100% dextran (gray diamonds) and 100% pullulan (black squares) assumption as a function of the phosphorus content.

3.2. Freeze-drying of the crosslinked hydrogels

3.2.1.Toward a better control of the supercooling degree

The hydrogel scaffolds were placed on the freeze-dryer trays either in contiguous or spaced configuration (isolated scaffolds) (**Fig. S4** in Supplementary materials). During the cooling stage of the freeze-drying, water solidified within the hydrogel scaffolds. In the absence of triggering, nucleation occurred spontaneously at significant supercooling, followed by ice growth near the ice melting point. In the spaced configuration, the nucleation temperature histogram is characterized by a mean of −13°C and a standard deviation of 3°C (Grenier et al., 2019). The nucleation is heterogeneous since the nucleation temperatures are much greater than the homogenous nucleation threshold of pure water (−35°C). For hydrogel scaffolds frozen in contiguous configuration, nucleation occurred in the scaffold with the highest nucleation temperature. It rapidly spread to all the scaffolds in the same Petri dish through the contact points between scaffolds. Propagation is so rapid (less than 100 ms, **Fig. S4 B** in Supplementary materials) that the scaffolds in the same dish start to freeze at about the same temperature. For packs of 50 contiguous scaffolds, nucleation occurred at supercooling

distributed around 9°C ± 1°C (**Fig. 3**). When the number of scaffolds per pack increases, the probability increases to find a scaffold with an intrinsic nucleation temperature exceeding a given value (between the mean value for isolated scaffolds, i.e., −13°C, and the ice melting point). Thus, the mean supercooling degree (i.e., the difference between the water freezing point and the temperature when freezing starts) of a pack of contiguous scaffolds is expected to decrease with the pack size.

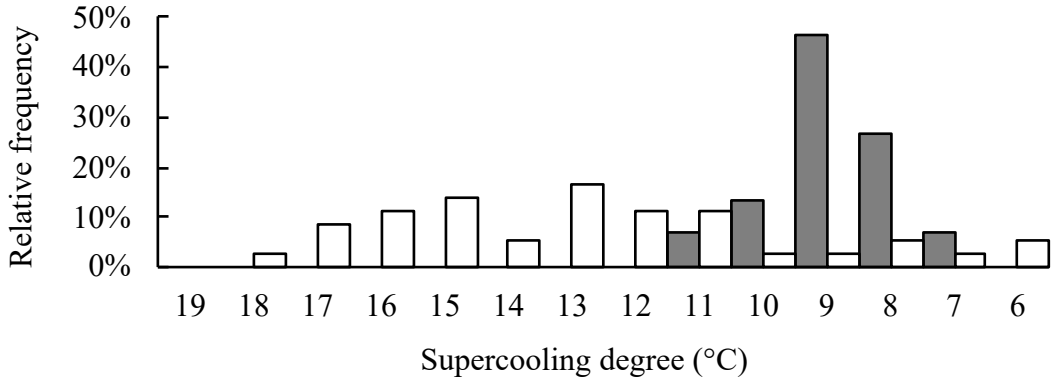

Fig. 3. Supercooling relative frequency for scaffolds freeze-dried in spaced configuration (white bars) and contiguous configuration (gray bars). In the latter case, scaffolds are in packs of 50 contiguous scaffolds. Crosslinker feed ratio $r = 96$ mol mol^{-1}.

At the end of freeze-drying, we systematically sorted the scaffolds according to their supercooling degree. In order to impose the supercooling degree (instead of undergoing it and sorting the scaffolds afterward), we developed a protocol inspired by the depressurization technique (Geidobler and Winter, 2013) to trigger the nucleation. Scaffolds were preliminarily arranged in spaced configuration or in packs of a few contiguous scaffolds. At the desired temperature during the cooling stage, a short pumping (during 30 s) followed by a vacuum break (via valve opening) induces a brief drop and rise of the pressure that triggers the nucleation in all scaffolds. In this way, we produce batches of scaffolds freeze-dried with supercooling degree set at 10°C. The standard deviation of the supercooling was 0.2°C. The

few scaffolds that froze before the short pumping event were systematically excluded from the study.

3.2.2. Effect of the crosslinker feed ratio on the scaffold microstructure

The supercooling degree was arbitrarily set at 10°C using the pressure variation protocol. The scaffolds were characterized at different stages of the process, i.e., after the cooling stage (frozen state), after sublimation (dry state), and after swelling. Different values of the feed ratio were investigated, i.e., r = 48, 72, 96, and 161 mol mol^{-1}. The case r = 0 mol mol^{-1} was approached by freezing at -10°C control drops (0.25 g.L^{-1} NaCl without polymer).

After the cooling stage and before sublimation, frozen samples with imposed supercooling degree of 10 ± 0.2°C were analyzed by electron cryo-microscopy equipped with EBSD. Crystal orientation map is displayed in the so-called Inverse Pole Figure (IPF). Ice grains are labeled according to the measured crystal orientation with respect to the reference direction parallel to the scaffold Z-axis (**Fig. 4A, B1-B4**). **Fig. 4A** shows the crystal orientation map for a control drop ($r = 0$ mol mol^{-1}). **Fig. 4B1-B4** give the crystal orientation map for frozen scaffolds with crosslinker feed ratio r = 48, 72, 96, and 161 mol mol^{-1}, respectively. EBSD data show that water solidified into hexagonal (Ih) ice. The solidified drop (**Fig. 4A**) essentially consists of a few crystals of millimetric size. The frozen scaffolds have a finer polycrystalline structure, with equiaxed morphology and texture (**Fig. 4B1-B4**). This morphology is expected when scaffolds are frozen at a low cooling rate, such as -0.1°C min^{-1} (O'Brien et al., 2004; Grenier et al., 2019). However, the c-axis pole figures reveal that high pole densities are obtained in or around Z-direction (see **Fig. S5** in Supplementary materials). Z-direction appears as one of the preferred orientations of the Ih-ice c-axis. This crystallographic orientation can be predominant (see **Fig. S5 B3** for instance), in agreement with the results reported in a precedent paper of the authors (Grenier et al., 2019).

The average grain size decreases with the crosslinker feed ratio, i.e., from 256 µm for r = 48 mol mol^{-1} down to 141 µm for r = 161 mol mol^{-1}. In the meantime, the interquartile range decreases from 217 µm to 113 µm and the 90th percentiles from 550 µm to 320 µm (**Fig. 4C**).

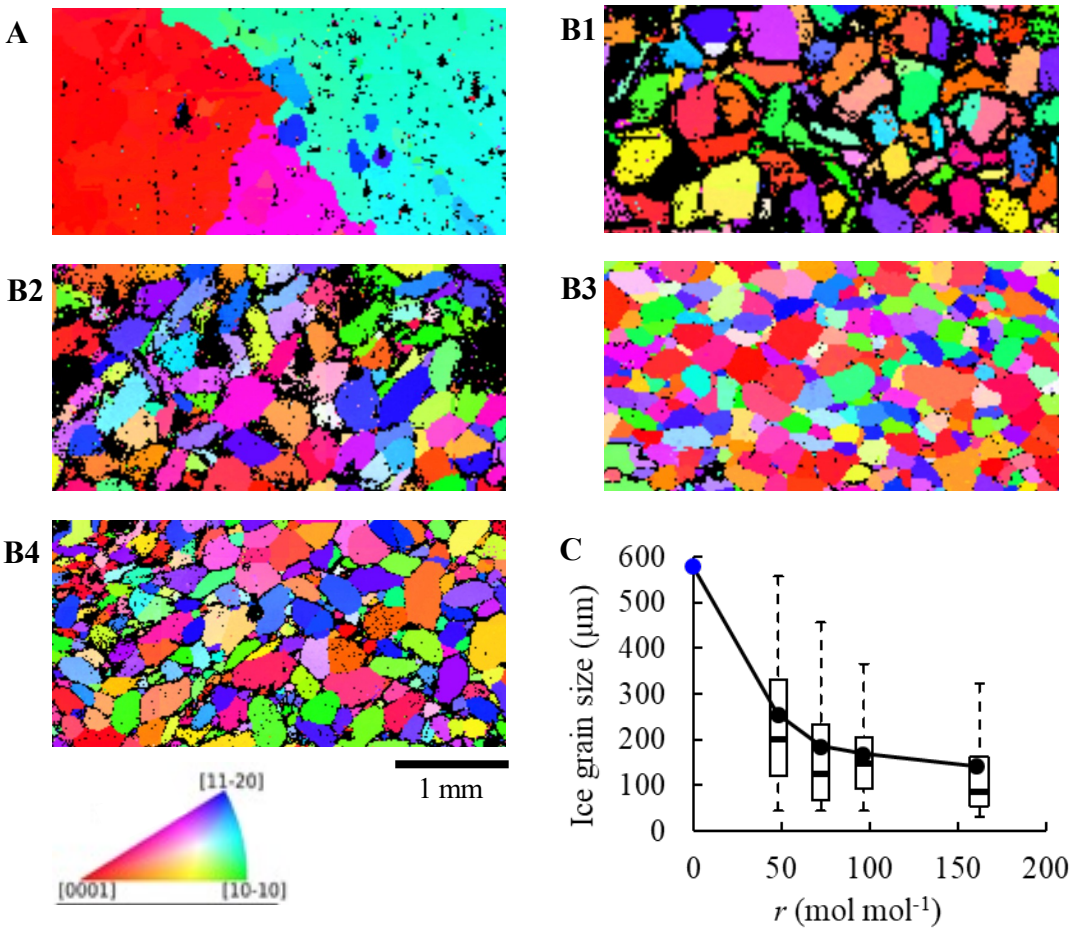

Fig. 4. Effect of the crosslinker feed ratio on the frozen scaffold microstructure. The supercooling degree was set at 10 ± 0.2°C. EBSD was performed at -100°C. **A:** Z-direction IPF coloring orientation map of an XY cross-section of a frozen 0.025% NaCl 120 µL drop standing for r = 0 mol mol^{-1}. **B1:** Orientation map of an XY cross-section of a frozen scaffold with crosslinker feed ratio r = 48 mol mol^{-1}. **B2:** r = 72 mol mol^{-1}. **B3:** r = 96 mol mol^{-1}. **B4:** r = 161 mol mol^{-1}. Red color corresponds to Ih-ice grains with crystallographic c-axis [0001] parallel to the Z-direction (see IPF key). Black color corresponds to domains which could not be indexed such as amorphous ice or cross-linked polymer. **C:** Variations of the mean ice grain

size as a function of the crosslinker feed ratio: frozen drop ($r = 0$ mol mol^{-1}, blue dot) and frozen hydrogel scaffolds (r = 48, 72, 96 and 161 mol mol^{-1}, dark dots). For the latter, the statistical summary of the ice grain size is provided as a box and whisker plot.

At the end of the whole freeze-drying process, the 3D porous structures were analyzed by X-ray computed tomography with a voxel size of (6 µm)^3. Typical XZ slices are reported in **Fig. 5** for increasing crosslinker feed ratio. We note that X-ray tomography provides high resolution imaging of the porous structure without the bias (such as perspective effect) encountered with Scanning Electron Microscopy. A 3D rendering from an X-ray tomography of a freeze-dried scaffold is displayed in **Fig. S6** in Supplementary materials.

The porosity of the scaffolds slightly decreases for increasing value of the crosslinker feed ratio, i.e., from 94±2% to 92±2% as r increases from 48 mol mol^{-1} to 161 mol.mol^{-1}. The pore size distribution in the dry state was obtained by image processing (**Fig. 6A1** and **Fig. S7**). They are similar regardless of the crosslinker feed ratio value (i.e., r = 48, 72, 96, or 161 mol mol^{-1}), and they are bimodal. The right peak of the distribution is broad, and its mean decreases with crosslinker feed ratio, i.e., from 280 µm (r = 48 mol mol^{-1}) to 200 µm (r = 161 mol mol^{-1}). The left peak of the distribution appears narrow and corresponds to pores with size lower than 65 µm. The frequency is maximal for the bin 0-15µm. The left peak population counts for a growing part of the total number of pores as the crosslinker feed ratio increases, i.e., from 8% for r = 48 mol mol^{-1} up to 40% for r = 161 mol mol^{-1}. However, even for the maximum value at r = 161 mol mol^{-1}, it represents only a tiny amount of the void fraction of a scaffold (less than 0.1%). These small pores are mainly located within the polymer walls forming the larger pores (right peak). The origin of the left peak will be discussed later. Overall, the number average pore size of the whole population (left and right peaks) ($\bar{d}_{pd}$) decreases linearly (R^2 = 0.984) with increasing crosslinker feed ratio, i.e., from 246 µm for r = 48 mol

mol^{-1} to 153 µm for r = 161 mol mol^{-1}. The comparison between **Fig. 4C** and **Fig. 6A2** shows that the number average pore size in the dry state coincides with the ice grain size. It confirms that most of the pores are formed from one to a few ice grains.

On average, the pores in the dry state are elongated: the mean Feret shape of the pores within a scaffold is 2.1 ± 0.5. This value varies little from one scaffold to another, i.e., between 1.9 and 2.2. The distribution of polar and azimuthal angles of pore major axis indicates that the major axis is preferred parallel to XY plane (see **Fig. S8** in Supplementary materials). This preferential orientation is more or less marked depending on the scaffold, independently of the crosslinker feed ratio. The median value of the pore inclination (defined as the pore major axis inclination to Z-direction) ranges from 52° to 71° (45° is attended in the absence of preferred orientation). The preferential orientation of the pore (major axis parallel to XY plane) is consistent with the preferred crystallographic orientation of the Ih-ice c-axis (parallel to Z) since ice crystal growth is faster in the (0001) basal plane (Nada & Furukawa, 2005) which presently coincides with the XY plane of the scaffolds.

When the freeze-dried scaffolds are hydrated in a physiological solution (DPBS), the polymer chains swell, and the pores shrink: for r = 96 mol mol^{-1} and supercooling degree of 10°C, the mean pore size decreases from 217 µm in the dry state (**Fig. 6A2**) to 82 µm in the swollen state (**Fig. 6A3**). **Fig. 6A3** shows that the mean pore size in the swollen state ($\bar{d}_{ps}$(DPBS)) decreases with the crosslinker feed ratio from 147 µm (r = 48 mol mol^{-1}) to 36 µm (r = 161 mol mol^{-1}) for a supercooling degree of 9°C ± 1°C. It appears that the pore shrinkage (presently defined as the ratio of the mean pore size in the dry state to the mean pore size in the swollen state) varies almost linearly with the crosslinker feed ratio, i.e., from 1.7 for r = 48 mol mol^{-1} to 4.2 for r = 161 mol mol^{-1}.

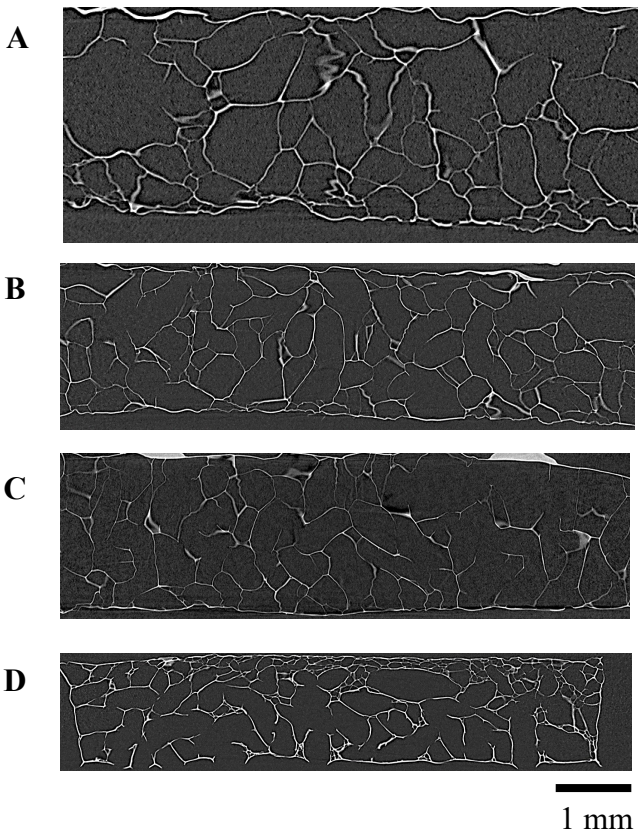

Fig. 5. XZ slices of freeze-dried hydrogel scaffolds acquired by X-ray tomography with 6-µm resolution. The supercooling degree (during freeze-drying) was set at 10 ± 0.2°C. Crosslinker feed ratio r = 48 mol mol^{-1} (**A**), r = 72 mol mol^{-1} (**B**), r = 96 mol mol^{-1} (**C**), and r = 161 mol mol^{-1} (**D**). Scale bar stands for 1 mm. The slices A to C are not whole in X-direction.

3.2.3. Effect of the supercooling degree on the scaffold microstructure

The influence of supercooling degree (ΔT) was investigated for hydrogel scaffolds synthesized with the crosslinker feed ratio r = 96 mol mol^{-1}. After freeze-drying, scaffolds were sorted according to the supercooling degree, i.e., from 6°C to 18°C, and were analyzed by X-ray computed tomography.

We occasionally examined some freeze-dried scaffolds using scanning electron microscopy (SEM): **Fig. S9** (see Supplementary materials) presents XY cross-sections of two scaffolds freeze-dried at different supercooling degrees. The mean pore size of the sample with the lowest supercooling degree seems greater. However, rigorous and reliable pore size analysis from these 2D images appears very difficult. This justify the use of X-ray computed tomography.

Fig. 6B1 and **Fig. S10** provide the pore size distributions obtained by X-ray tomography. It can be observed that the pore size distributions are bimodal. The left peak (**Fig. 6B1**) corresponds to pore size between 30 µm and 150 µm. In this part of the spectrum, the frequency is maximal for the bin 75-90 µm, and its value increases with the supercooling degree. The right peak corresponds to a pore size greater than 150 µm. The peak broadens as the supercooling degree decreases. The pore size corresponding to the maximum frequency shifts from 225 µm to 270 µm as the supercooling degree decreases from 18°C to 6°C. It should be noted that the right and left peaks overlap between 100 µm and 180 µm. Consequently, the left peak is hardly visible for the lowest supercooling degree ΔT = 6°C.

The overlap makes it difficult to quantify each population. However, the weight of the left peak population may be estimated assuming that this population is symmetric with respect to the bin 75-90 µm. Under this hypothesis, the left peak population represents from 25% to 40% of the total number of pores as the supercooling degree increases from ΔT = 11°C to ΔT = 18°C. This population corresponds to a few percent of the total porosity of a freeze-dried scaffold, i.e., from 2% for ΔT = 11°C to 8% for ΔT = 18°C.

Fig. 6B2 shows that the mean pore size (obtained by averaging over the whole spectrum) of the freeze-dried scaffolds decreases linearly (R^2 = 0.904) with the supercooling degree, i.e., from 243 µm for ΔT = 6°C to 167 µm for ΔT = 18°C. We note that the scaffolds with ΔT =

11°C deviate from this linear trend. They come from the same fabrication lot. The correlation coefficient is significantly better if we discard it, i.e., $R^2 = 0.99$.

These results are in line with the reported effect of nucleation temperature on primary drying rate during lyophilization: it was found that the lower the nucleation temperature, the lower the effective pore radius, and the lower the primary drying rate (Konstantinidis et al., 2011; Searles et al., 2001).

We also characterized the pore morphology and orientation: on average, the pores are elongated with a mean Feret shape of 2.1 ± 0.5. This value varies slightly (between 2.0 and 2.2) from one scaffold to the other without any correlation with the supercooling degree. The pores are slightly preferred parallel to the XY plane. Depending on the scaffold, the median value of the pore inclination to the Z-direction ranges from 52° to 71°. No correlation emerges between the pore orientation and the supercooling degree.

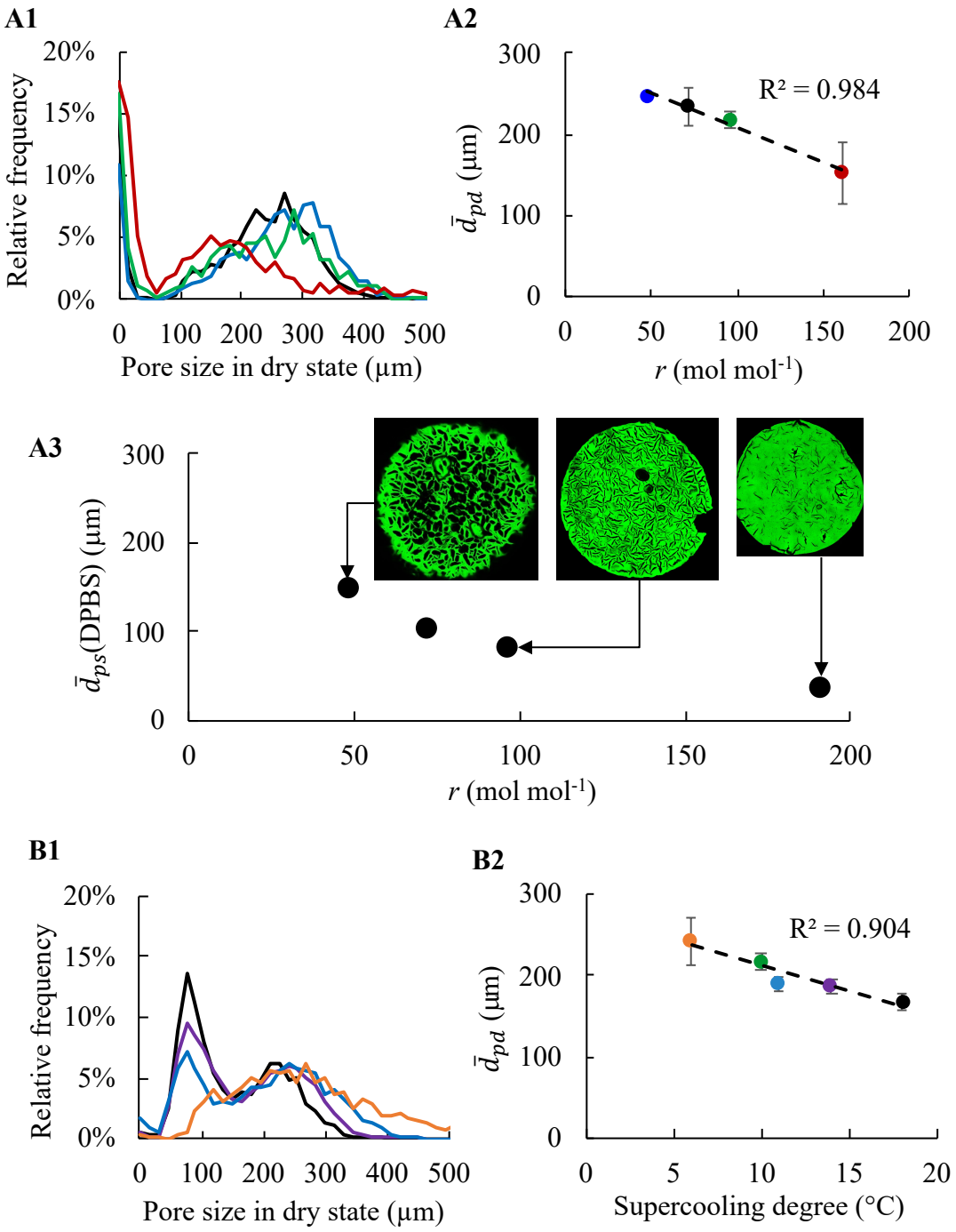

Fig. 6. Pore structure characterization of the freeze-dried scaffolds. Scaffolds in the dry state were fully analyzed by X-ray computed tomography with (6 µm)^3 voxel size. Scaffolds in the swollen state were analyzed using Confocal Laser Scanning Microscopy. **A**: Effect of the crosslinker feed ratio on the porous structure. **A1, A2**: The supercooling degree (during freeze-drying) was set at 10 ± 0.2°C for the 4 values of the crosslinker feed ratio. **A3**: The supercooling

degree was 9°C ± 1°C for the 4 values of the crosslinker feed ratio. **A1**: Pore size distribution in the dry state for r = 48 mol mol^{-1} (blue line), r = 72 mol mol^{-1} (black line), r = 96 mol mol^{-1} (green line), and r = 161 mol mol^{-1} (red line). **A2**: Mean pore size in dry state as a function of the crosslinker feed ratio. **A3:** Mean pore size of the scaffolds swollen in DPBS as a function the crosslinker feed ratio, CLSM XY cross-sections for r = 48, 96 and 161 mol mol^{-1} (the diameter of the swollen scaffolds is 7.7 mm, 7.5 mm, and 6.5 mm, respectively).

B: Effect of the supercooling degree on the porous structure in the dry state. The crosslinker feed ratio was set at r = 96 mol mol^{-1}. **B1**: Pore size distribution in the dry state for supercooling degree ΔT = 6°C (orange line), ΔT = 11°C (blue line), ΔT = 14°C (purple line) and ΔT = 18°C (black line). **B2**: Mean pore size in the dry state as a function of the supercooling degree. The green dot that corresponds to r = 96 mol mol^{-1} and ΔT = 10°C is also displayed in **A2**.

3.3. Infiltration and seeding ability of freeze-dried scaffolds

The infiltration ability of the freeze-dried FITC-labelled scaffold was quantified using narrow-sized calibrated fluorescent red polyethylene rigid microspheres of various sizes suspended in DPBS. As soon as the microsphere suspension is deposited on top of the freeze-dried scaffolds, the scaffolds start to shrink (even if, at the same time, the polymer swelled from the dry state). As the liquid is sucked in, microspheres enter the pores. After complete swelling of the scaffolds (achieved by further addition of DPBS without microspheres), the size of the scaffolds was smaller than in the dry state. Indeed, the scaffolds were freeze-dried after swelling in NaCl (0.25 g.L^{-1}), and the swelling ratio of the hydrogel in this solvent is about three times higher than in DPBS (Grenier et al., 2019).

Confocal Laser Scanning Microscopy (CLSM) analysis shows that the microspheres infiltrated the scaffolds over their entire 1.6-mm depth (**Fig. 7A**). However, the microspheres did not

infiltrate every pore (**Fig. 7A**). One reason is that the microspheres cannot enter pores smaller than their diameter. This phenomenon may be highlighted by the calculation of the exclusion coefficient (F) defined as the ratio of the mean size of the occupied pores (by microspheres) to the overall mean pore size (both sizes are measured in the swollen state). **Fig. 7B** reports the variations of the exclusion coefficient as a function of the microsphere diameter for scaffolds characterized by $r = 96$ mol mol^{-1} and $\Delta T = 9°C \pm 1°C$. The mean pore size in the dry state measured by X-ray computed tomography was 230 ± 20 µm. The exclusion coefficient is theoretically equal to 1 for diameters tending to 0. We observed that the exclusion coefficient remains close to 1 for microsphere diameter up to $d_s = 15$ µm but reaches 3.3 for $d_s = 58$ µm and 4.4 for $d_s = 115$ µm. As d_s increases, microspheres segregate in ever-larger pores. For $d_s = 115$ µm, the mean size of the occupied pores is equal to 180 µm. Since it is only 60% greater than the microsphere diameter, the microspheres are encased in the pores as shown in **Fig. 7A**.

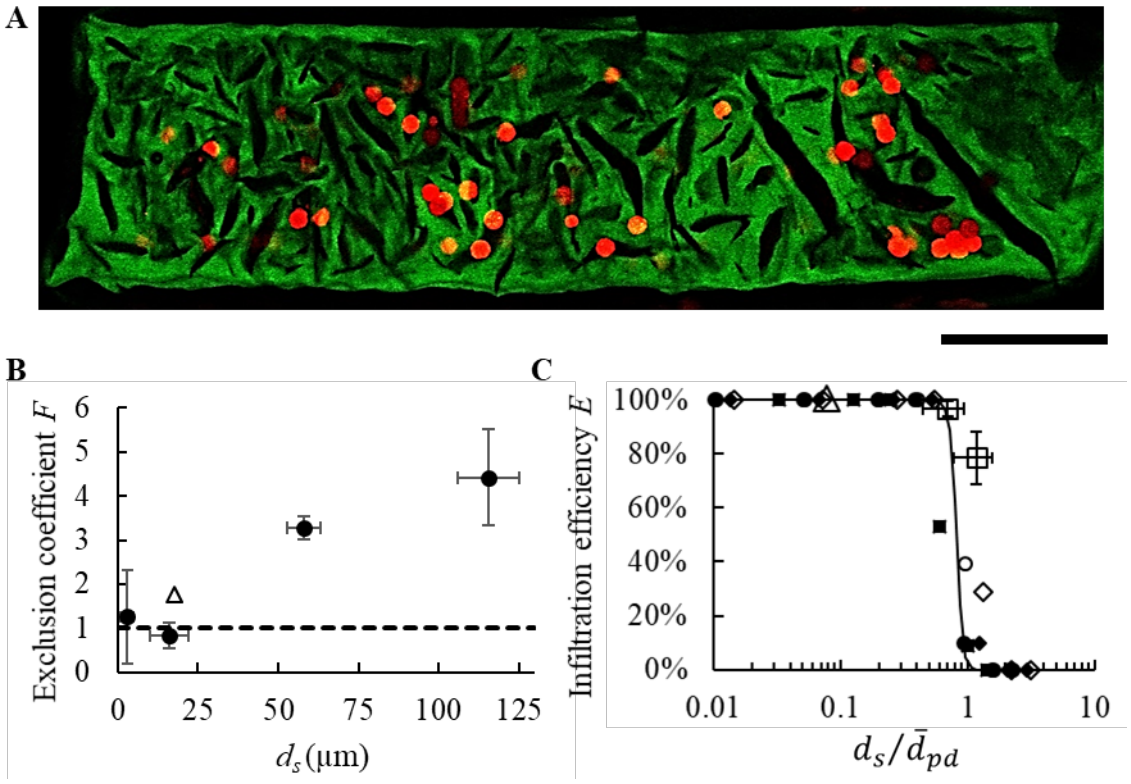

Fig. 7. Infiltration of FITC-labelled freeze-dried scaffold. **A**: CLSM XZ cross-section of a scaffold (230 ± 20 µm of mean pore size in the dry state) infiltrated with microspheres (115 ± 15 µm in diameter). The scale bar represents 1 mm. **B**: Exclusion coefficient as a function of the microsphere diameter (●), exclusion coefficient determined for the osteoblasts (△). The dashed line corresponds to the theoretical value of the exclusion coefficient when the microsphere diameter is much less than the mean pore size. **C**: Infiltration efficiency as a function of the ratio of the microsphere diameter to the mean pore size in the dry state. Narrow-sized calibrated microspheres of diameter 3 ± 1 µm, 15 ± 5 µm, 58 ± 5 µm, 115 ± 10 µm, 275 ± 25 µm, 463 ± 38 µm, and 655 ± 55 µm. Scaffolds with mean pore size in the dry state of 208 µm (◇), 221 µm, (◆) 285 µm (○), 295 µm (●), and 460 µm (■). Data were fitted by a hyperbolic tangent (solid line) using least squares method. Seeding efficiencies of osteoblast (△) and hepatocyte spheroids (□) on freeze-dried scaffolds (mean pore size in the dry state of 230 µm) are also reported on the graph.

The infiltration efficiency (*E)* was measured for scaffolds with mean pore size in the dry state of 208, 221, 285, 295, and 460 µm, using microspheres with diameters ranging between 3 µm and 655 µm, i.e., over two orders of magnitude. It appears that the variations of the seeding efficiency can be plotted into the same curve when expressed as a function of the ratio of the microsphere diameter to the mean pore size in the dry state (**Fig. 7C**). We observe a sharp transition from 100%-efficiency to 0%-efficiency as the microsphere to mean pore size ratio increases, i.e., while the microsphere diameter becomes larger than the dried mean pore size.

Finally, the seeding ability of the freeze-dried scaffolds was quantified for (i) individual (non-aggregated) osteoblast cells (MC3T3-E1) and (ii) hepatocyte spheroids (HepaRG^{TM}) (**Fig. 8**). The seeding efficiency of individual osteoblast cells (18 µm in diameter) on freeze-dried scaffolds with mean pore size in dry state between 100 and 295 µm was systematically equal to 100%. This result is consistent with the measurements performed with microspheres of equivalent diameter d_s = 15 µm. For scaffolds with mean pore size in dry state equal to 230 µm, the exclusion coefficient was equal to 1.76, slightly greater than the value (close to 1) measured with the microspheres (**Fig. 7B**).The hepatocyte spheroids were an order of magnitude greater in size than individual osteoblasts (**Fig. 8**) and were chosen so that their sizes were in the range of pore sizes of dry scaffolds. The seeding efficiency was measured on scaffolds with a mean dry pore size of 208 µm. *E* was found to be equal to 97 ± 3 for 145 µm-spheroids, and to 78 ± 10 for 245 µm-spheroids. These efficiency values are slightly greater than the efficiency values measured with rigid synthetic microspheres of equivalent diameters (**Fig. 7C**), likely due to the deformability of spheroids which facilitated their entry into the pores.

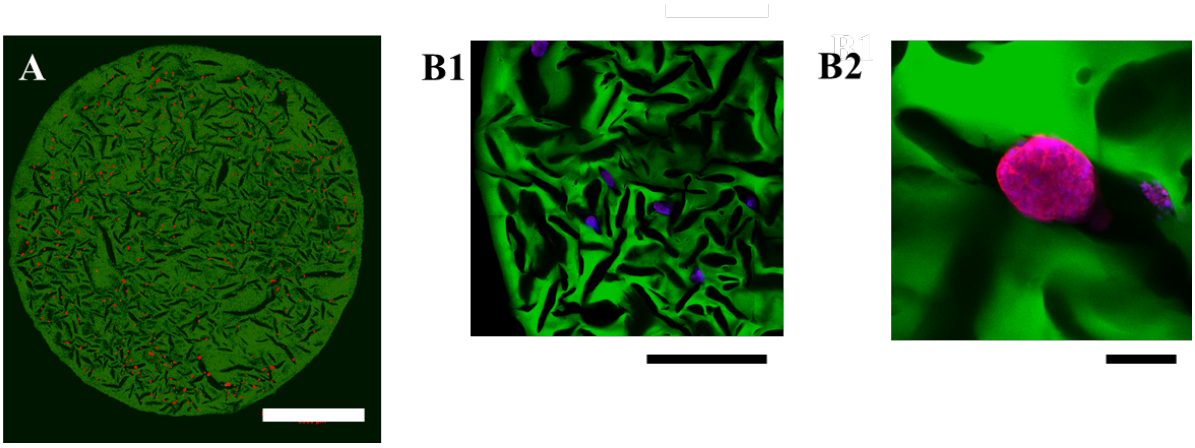

Fig. 8. Cell organisation after seeding on the freeze-dried scaffolds. **A**: CLSM XY cross-section of a whole scaffold after cell seeding with individual osteoblastic cells. Mean pore size in the dry state of 230 µm. Red channel corresponds to PKH26 red dye cell membrane labeling, green channel to the FITC loaded scaffold. The scale bar stands for 2 mm. **B**: CLSM image of HepaRG™ spheroids of 150-µm diameter entrapped in a hydrogel scaffold with a mean pore size in dry state of 230 µm. Cell nuclei were stained with DAPI and actin cytoskeletons with TRITC-Phalloidin. **B1**: The scale bar stands for 1 mm. **B2**: The scale bar stands for 100 µm.

4. Discussion

4.1. Impact of chemical conditions on crosslinked polysaccharide hydrogels

The crosslinking of polysaccharide chains in aqueous sodium hydroxide occurs as follows: STMP first reacts with the alcoholate of the polysaccharide chains to give grafted sodium tripolyphosphate (Lack et al., 2004). Then, this group may react either with the alcoholate of another chain to form an intermolecular phosphodiester bond or with an alcoholate belonging to the same chain to form an intramolecular phosphodiester bond or with NaOH to form a phosphate monoester. The intermolecular phosphodiester bonds are the efficient links behind the chemical network. The density of these bonds thus conditions the hydrogel elasticity.

The monitoring of the crosslinking at 50°C by oscillatory rheology showed that the storage modulus of the polymer mixture (G') increases rapidly during the first minutes of the process and then slightly decreases (**Fig. 1**). This non-monotonous behavior suggests that two phenomena are competing, i.e., the rapid formation of crosslinks and their slower degradation due to the very aggressive character of the reaction medium (Lack et al., 2007). This degradation corresponds to the conversion of intermolecular phosphodiester bonds into phosphate monoesters.

An estimate of the crosslinking characteristic time is given by the time (t_{max}) for the storage modulus to reach its maximal value. This time is two orders of magnitude lower than the characteristic time of the order of 10^3 min (estimated from the variations of STMP concentration as a function of time) previously reported by Lack et al. (Lack et al., 2007). The difference is due to the high alkalinity of our reaction medium, which increases the reactivity of the polysaccharide chains (the proportion of alcoholates increases with the pH), and to the high temperature, which increases the mobility of STMP and polymer chains (Lack et al., 2004). On the other hand, the crosslinking characteristic time increases with the crosslinker feed ratio (**Fig. S2**). Indeed, a greater STMP feed ratio allows greater crosslinking degrees, and the mobility of the polymer chains decreases as the crosslinking degree increases. For the highest value of STMP feed ratio $r = 161$ mol mol^{-1}, the crosslinking characteristic time is close to 12 min, a value compatible with industrial productivity constraints.

The alkalinity also strongly influences the ratio of the phosphate implied in intermolecular crosslinks to the total incorporated phosphate in the final hydrogel. This ratio is equal to about 5% in the present experiments (**Fig. 2C** and section **3.1**), i.e., one order of magnitude lower than previously reported in other conditions (Dulong et al., 2011). 95% of the total incorporated phosphate corresponds to phosphate monoesters. Since the degradation kinetics of phosphate

diesters is slow, we expect that most of the phosphate monoesters are formed when grafted sodium tripolyphosphate reacts with NaOH (Lack et al., 2007).

4.2. Swelling behavior and solvent selection for freeze-drying

Both phosphate monoesters and phosphate diesters bring negative charges to the polymer network. However, phosphate monoesters are the main contributors because these groups are presently more abundant than phosphate diesters. Furthermore, phosphate monoesters are doubly-charged, whereas phosphate diesters are singly-charged. The electric charge carried by the polymer chains makes the hydrogel scaffolds very sensitive to the ionic strength of the solvent. In NaCl (0.25 g L^{-1}), the ionic strength is low, i.e., 4 10^{-3} M, and the strong repulsive interactions between the negatively charged groups induce a large swelling ratio (**Fig. 2C**). The ionic strength of DPBS is larger, i.e., 2 10^{-1} M, and the repulsive interactions between the negatively charged groups are efficiently screened by the ions of the solvent, and the swelling ratio is comparatively smaller (**Fig. S3**).

As the crosslinker feed ratio used for the hydrogel preparation increases (i.e., from 0.049 to 0.163 mol L^{-1}), the phosphorus content of the final hydrogel increases (**Fig. 2A**), the number of intermolecular crosslinks per primary molecule increases as well (**Fig. 2C**), and the swelling ratio decreases for a given solvent (see **Fig. 2E** for NaCl 0.25 g L^{-1} and **Fig. S3** for DPBS). We deduce that the increase in crosslink density dominates the effect of the increase in overall charge. This behavior is consistent with results of the literature obtained with low amounts of STMP, i.e., from 0 to about 0.1 mol.L^{-1} (Dulong et al., 2011). Above that range, an increase in the swelling ratio is observed, attributed to the increase in the negative charges brought by the monolinked phosphorus (mainly grafted tripolyphosphate in this case) (Dulong et al., 2011).

Suppose we neglect the changes in scaffold size (disk diameter and thickness) during the freeze-drying step. In that case, we may infer that the higher the swelling ratio, the higher the

porosity of the final dried scaffold and the larger the mean pore size in the dry state ($\bar{d}_{pd}$). Thus, the ionic strength of the freeze-drying solvent appears as a parameter able to tune the mean pore size in the dry state. The lower the ionic strength, the larger the mean pore size in the dry state and the stronger the shrinkage of the scaffold from the dry state to the swollen state in DPBS.

4.3. Crosslinker feed ratio and supercooling degree modulate mean pore size

The freezing of a scaffold proceeds in three steps, i.e. (1) primary nucleation of ice crystals in the supercooled hydrogel, (2) secondary nucleation encompassing the entire scaffold (during recalescence, i.e., when scaffold temperature relaxes to ice melting point consequently to the release of latent heat), (3) grain growth near the ice melting point until complete solidification. We previously demonstrated that the primary nucleation is heterogenous and singular (Dantzig and Rappaz, 2016; Grenier et al., 2019; Vali, 1994). Each scaffold contains only a few nucleating sites, i.e., 0.1 nuclei cm^{-3} $°C^{-1}$, and each site is characterized by its own activation temperature (Grenier et al., 2019). For an isolated scaffold, freezing starts from the nucleating site with the highest activation temperature as soon as the hydrogel reaches this temperature during cooling. This temperature is the nucleation temperature of the isolated scaffold. The supercooling is generally large at the onset of freezing (mean value of 13°C for isolated scaffolds), and growing ice crystals are expected to be needle-like (Shibkov et al., 2003). During recalescence, the ice needles grow rapidly through the scaffold. Due to the constraints exerted by the surrounding nano-scale polymer network (of mesh size ξ_s), the needles may detach from the needled-branch structure or shatter. The detached needles or the needle fragments act as secondary nuclei (Agrawal and Paterson, 2015; K. M. Pawelec et al., 2014a). Most of the ice grains (observed after complete solidification) result from secondary nucleation.

The proposed mechanism for secondary nucleation is consistent with the observed effects of crosslinker feed ratio on mean pore size in the dry state. The underlying assumption is that the higher the crosslinker feed ratio, the more nucleation centers (Amirian et al., 2020). Indeed, the higher the crosslinker feed ratio, the lower the network mesh size (ξ_s), the higher the shear modulus and the mechanical constraints exerted by the polymer network on the growing ice needles. Then, ice needle detachment or fragmentation is more frequent, and secondary nuclei are more numerous. This phenomenon leads to a finer polycrystalline structure, smaller ice grain size (**Fig. 4C**), and smaller mean pore size in the dry state (**Fig. 6A2**). It should be noted that the mesh size in the swollen state (ξ_s) decreases with r because the number of intermolecular crosslinks per primary molecules increases and also because the swelling ratio (Q) subsequently decreases.

Furthermore, it is well established that the tip radii of ice crystals growing in supercooled water decrease as the supercooling increases (Furukawa and Shimada, 1993; Shibkov et al., 2005). The mean radius of the ice needles and the needle spacing decrease as well. Since needles are thinner and more numerous, their detachment or fragmentation is more frequent, and ensuing secondary nucleation is enhanced (at fixed crosslinker feed ratio). A finer polycrystalline structure is thus expected for the scaffolds with greater nucleation temperature, leading to a lower mean pore size in the dry state. This is actually confirmed by the results presented on **Fig. 6B2**. It should be noted that the way primary nucleation occurs (either spontaneously at the proper nucleation temperature of the scaffold, or driven by another contiguous frozen scaffold, or triggered by a brief pressure variation) does not affect the conclusions drawn above. The critical parameter is the supercooling reached by the scaffold at the onset of freezing.

4.4. Bimodal pore size distribution

The existence of two peaks or modes within the pore size spectrum in the dry state and their distinctive responses to changes in parameters (see **Fig. 6A1** and **Fig. 6B1**) suggested that their physical origin is different: whereas the right peak population with greater mean pore size corresponds to the sublimation of ice grains, we propose that the left peak corresponds to the formation of air bubbles at the end of solidification. Indeed, since the solubility of air is much lower in ice than in liquid water, dissolved air is rejected in the intergranular liquid as solidification proceeds. When the supersaturation of air in the intergranular liquid is high enough, bubbles appear and grow. The volume fraction associated with the left peak population (estimated at 2% for supercooling degree ΔT = 11°C and at 8% for ΔT = 18°C) is consistent with the bubble volume fraction reported by Chu et al. (Chu et al., 2019) for freezing droplets, i.e., 5.67±1.5 % for ΔT = 20°C.

Air solubility in liquid water increases with decreasing water temperature, i.e., from 3% volume fraction at 0°C to 6.53±1.68 % at −20°C (Chu et al., 2019). Since hydrogel swollen in NaCl (0.25 g L^{-1}) consists mainly of water, the same trend can be reasonably expected for air solubility in the hydrogel, explaining why the volume fraction associated with the left peak increases with the scaffold supercooling degree.

When freezing is triggered by a brief pressure variation (protocol used to impose the supercooling degree when studying the effect of the crosslinker feed ratio), scaffolds are expected to degas during the pumping phase. The amount of dissolved air at the onset of freezing is thus lower, explaining why the volume fraction associated with the left peak decreases from a few percent when nucleation is spontaneous to less than 0.1% when the pressure variation protocol is used. In addition, **Fig. S7** shows that the right peak, associated

with the sublimation of ice grains, remains the same, with or without pressure variation protocol.

4.5. Infiltration threshold

In biomedical applications, cell seeding is typically performed on dry scaffolds. Indeed, in the dry state, the mean pore size of the scaffolds and the connectivity between pores are maximized. Here, the mean pore size in the dry state is about five times greater than the mean pore size when swollen in DPBS. A soon as the seeding suspension is deposited on a dry scaffold, capillarity drains the suspension inside the scaffold. Depending on their size, the biological entities may either follow the liquid and enter the pores, or be rejected at the pore entrance.

Since the penetration of the suspension into the pores is concomitant with the swelling of the hydrogel, it is difficult to evidence between the mean pore size in the dry state and the mean pore size in the swollen state, which one truly controls the seeding. The infiltration tests performed with narrow-sized calibrated synthetic rigid microspheres helped answer this question. Such beads are primarily used for membrane filter testing, i.e., to estimate the membrane pore size and determine its retention capabilities. These beads have the advantage of being well-characterized and available in a wide range of sizes. The use of beads allows us to first focus on a single parameter, their size, independently of the complexity and variability inherent to the use of cells or cellular spheroids. We found that the infiltration efficiency (E) depends on only one parameter, i.e., the ratio of the microsphere diameter to the mean pore size in the dry state ($d_s/\bar{d}_{pd}$). Indeed, all the data collapse into one single curve when expressed as a function of this ratio (**Fig. 7C**). This master curve is characteristic of the present scaffold family. The curve's steepness indicates a sharp transition from 100%-efficiency to 0%-efficiency as the microsphere to mean pore size ratio increases. A relevant function to describe

such a transition is the hyperbolic tangent. We found that the following law well fits the experimental points:

$$E = 0.5 - 0.5 \tanh\left(\frac{\left(d_s/\bar{d}_{pd}\right) - 0.82}{0.096}\right) \quad (3)$$

We deduce that the transition threshold corresponds to $d_s = 0.82\ \bar{d}_{pd}$ and that the width of the transition is narrow and equal to $0.048\ \bar{d}_{pd}$: the mean pore size in the dry state is thus the scaffold morphological parameter that controls the seeding.

The seeding efficiency for cells or cellular spheroids can be reasonably estimated from the microsphere infiltration master curve (**Fig. 7C**). We only noticed some slight discrepancies between microspheres and spheroids data close to the transition threshold. We expect that the deformability of the spheroids helps their entry into the pores.

Eventually, we demonstrated the feasibility of seeding hepatocyte spheroids in scaffolds with the appropriate pore size, which may provide another route to cultivate hepatocytes in a 3D microenvironment (Labour et al., 2020).

5. Conclusion

We found that the porous structure of a thin hydrogel scaffold freeze-dried at a low cooling rate is highly correlated with the supercooling degree reached by the scaffold at the onset of freezing. The scaffold mean pore size decreases linearly from 240 to 170 μm for the polysaccharide-based hydrogel of the present study when the supercooling degree increases from 6 to 18°C.

We evidenced that the control of supercooling requires to trigger the nucleation of ice, and this triggering must be performed at sufficiently low supercooling, i.e. before potential spontaneous nucleation events within the scaffold batches. In absence of triggering, the effect of

supercooling degree on mean pore size is responsible for mean pore size variability within a batch and from batch to batch.

At a fixed supercooling degree, the pore morphology can be tuned by varying the crosslinker feed ratio. We fixed the supercooling degree at 10°C and found that the mean pore size in the dry state decreases from 250 to 150 μm as the number of intermolecular crosslinks per primary molecule increases from 3 to 7. The intermolecular crosslinks represent about 5% of the total incorporated phosphate whereas the remaining 95% only contribute to the electric charge of the hydrogel.

The effect of crosslinker feed ratio and supercooling degree on scaffold porous morphology can be explained from the interactions between the needle-like primary ice crystals and the surrounding polymer network. As the supercooling degree increases, the primary ice needles are thinner and the needle spacing is lower. The detachment of needles from the needle-branched structure is more frequent and the secondary nuclei are more numerous. Ultimately, the ice grain size of the frozen scaffold is lower and the mean pore size of the freeze-dried scaffold as well.

The scaffold mean pore size in the dry state is also affected by the freeze-drying solvent. Indeed, since STMP crosslinking brings electric charge to the polymer network, the hydrogel scaffolds is sensitive to the ionic strength of the solvent. As the ionic strength decreases, the hydrogel swelling ratio increases. Then, the ice grain size increase and the mean pore size in dry state as well. Thus, the ionic strength of the freeze-drying solvent appears as another parameter to tune the mean pore size in the dry state.

The infiltration efficiency of the freeze-dried scaffolds was quantified both with suspensions of narrow-sized calibrated microspheres and with suspensions of biological objects, i.e. cells and spheroids. All the data collapse into one single curve when the efficiency is expressed as a

function of the ratio of the diameter to the mean pore size in dry state. Even if the swelling of the hydrogel occurs concomitantly with the penetration of the suspension into the pores, the seeding is rather conditioned by the mean pore size in dry state than by the mean pore size in swollen state.

As the ionic strength of the freeze-drying solvent is lower than the ionic strength of typical physiological solvents such as DPBS, scaffolds shrink when impregnated with a suspension of biological objects. We expect that the shrinkage (which can be modulated by adjusting the ionic strength of the freeze-drying solvent) enhances the trapping within the porous structure.

Altogether, we can thus precisely tune the porosity of these 3D materials of high interest for 3D cell culture, and for production of cGMP scaffolds for tissue engineering applications.

Declaration of competing interest

DL has shares in SILTISS company that holds 4 patents on these scaffolds for tissue engineering.

Acknowledgements

This work is supported by the “IDI 2016” project funded by the IDEX Paris-Saclay, ANR-11-IDEX-0003-02, by the LabEx LaSIPS (ANR-10-LABX-0032-LaSIPS) managed by the French National Research Agency under the "Investissements d'avenir" program (ANR-11-IDEX-0003), and by “Recherche Hospitalo-universitaire” Innovations for Liver Tissue Engineering (RHU iLite), grant number ANR-16-RHUS-0005. The authors acknowledge the 3D-BioMat project hosted by the CEBB (Pomacle, F-51110), that is co-financed by the Grand Reims and the European Union, committed to the Grand Est with the European Regional Development Fund.

Supplementary materials

Supplementary materials to this article can be found online.

References

Agrawal, S.G., Paterson, A.H.J., 2015. Secondary Nucleation: Mechanisms and Models. Chem. Eng. Commun. 202, 698–706. https://doi.org/10.1080/00986445.2014.969369

Amirian, J., Zeng, Y., Shekh, M.I., Sharma, G., Stadler, F.J., Song, J., Du, B., Zhu, Y., 2020. In-situ crosslinked hydrogel based on amidated pectin/oxidized chitosan as potential wound dressing for skin repairing. Carbohydr. Polym. 117005. https://doi.org/10.1016/j.carbpol.2020.117005

Autissier, A., Le Visage, C., Pouzet, C., Chaubet, F., Letourneur, D., 2010. Fabrication of porous polysaccharide-based scaffolds using a combined freeze-drying/cross-linking process. Acta Biomater. 6, 3640–3648. https://doi.org/10.1016/j.actbio.2010.03.004

Bai, H., Chen, Y., Delattre, B., Tomsia, A.P., Ritchie, R.O., 2015. Bioinspired large-scale aligned porous materials assembled with dual temperature gradients. Sci. Adv. 1, e1500849. https://doi.org/10.1126/sciadv.1500849

Bell, C.C., Hendriks, D.F.G., Moro, S.M.L., Ellis, E., Walsh, J., Renblom, A., Fredriksson Puigvert, L., Dankers, A.C.A., Jacobs, F., Snoeys, J., Sison-Young, R.L., Jenkins, R.E., Nordling, Å., Mkrtchian, S., Park, B.K., Kitteringham, N.R., Goldring, C.E.P., Lauschke, V.M., Ingelman-Sundberg, M., 2016. Characterization of primary human hepatocyte spheroids as a model system for drug-induced liver injury, liver function and disease. Sci. Rep. 6, 25187. https://doi.org/10.1038/srep25187

Berthiaume, F., Maguire, T.J., Yarmush, M.L., 2011. Tissue engineering and regenerative medicine: history, progress, and challenges. Annu. Rev. Chem. Biomol. Eng. 2, 403–430. https://doi.org/10.1146/annurev-chembioeng-061010-114257

Campbell, J.J., Husmann, A., Hume, R.D., Watson, C.J., Cameron, R.E., 2017. Development of three-dimensional collagen scaffolds with controlled architecture for cell migration studies using breast cancer cell lines. Biomaterials 114, 34–43. https://doi.org/10.1016/j.biomaterials.2016.10.048

Canal, T., Peppas, N.A., 1989. Correlation between mesh size and equilibrium degree of swelling of polymeric networks. J. Biomed. Mater. Res. 23, 1183–1193. https://doi.org/10.1002/jbm.820231007

Chambon, F., Winter, H.H., 1987. Linear Viscoelasticity at the Gel Point of a Crosslinking PDMS with Imbalanced Stoichiometry. J. Rheol. 31, 683–697. https://doi.org/10.1122/1.549955

Chaouat, M., Le Visage, C., Autissier, A., Chaubet, F., Letourneur, D., 2006. The evaluation of a small-diameter polysaccharide-based arterial graft in rats. Biomaterials 27, 5546–5553. https://doi.org/10.1016/j.biomaterials.2006.06.032

Chu, F., Zhang, X., Li, S., Jin, H., Zhang, J., Wu, X., Wen, D., 2019. Bubble formation in freezing droplets. Phys. Rev. Fluids 4, 071601. https://doi.org/10.1103/PhysRevFluids.4.071601

Chuang, E.Y., Chiang, C.W., Wong, P.C., Chen C.H., 2018. Hydrogels for the Application of Articular Cartilage Tissue Engineering: A Review of Hydrogels. Advances in Materials Science and Engineering, Article ID 4368910, 13 pages. https://doi.org/10.1155/2018/4368910

Chung, T.W., Yang, J., Akaike, T., Cho, K.Y., Nah, J.W., Kim, S.I., Cho, C.S., 2002. Preparation of alginate/galactosylated chitosan scaffold for hepatocyte attachment. Biomaterials 23, 2827–2834. https://doi.org/10.1016/s0142-9612(01)00399-4

Dantzig, J.A., Rappaz, M., 2016. Solidification: 2nd Edition - Revised & Expanded. EPFL Press.

de Gennes, P.-G., 1979. Scaling Concepts in Polymer Physics. Cornell University Press.

Deville, S., 2010. Freeze-Casting of Porous Biomaterials: Structure, Properties and Opportunities. Materials 3, 1913–1927. https://doi.org/10.3390/ma3031913

Deville, S., Saiz, E., Nalla, R.K., Tomsia, A.P., 2006. Freezing as a Path to Build Complex Composites 311, 515–518. https://doi.org/10.1126/science.1120937

DeVolder, R., Kong, H.J., 2012. Hydrogels for in vivo-like three-dimensional cellular studies. WIREs Syst Biol Med 4, 351–365. doi: 10.1002/wsbm.1174

Drury, J.L., Mooney, D.J., 2003. Hydrogels for tissue engineering: scaffold design variables and applications. Biomaterials 24, 4337–4351. https://doi.org/10.1016/S0142-9612(03)00340-5

Dulong, V., Forbice, R., Condamine, E., Le Cerf, D., Picton, L., 2011. Pullulan–STMP hydrogels: a way to correlate crosslinking mechanism, structure and physicochemical properties. Polym. Bull. 67, 455–466. https://doi.org/10.1007/s00289-010-0435-2

Flory, P.J., 1953. Principles of polymer chemistry, Ithaca, N.Y. : Cornell University Press. ed.

Fricain, J.C., Schlaubitz, S., Le Visage, C., Arnault, I., Derkaoui, S.M., Siadous, R., Catros, S., Lalande, C., Bareille, R., Renard, M., Fabre, T., Cornet, S., Durand, M., Léonard, A., Sahraoui, N., Letourneur, D., Amédée, J., 2013. A nano-hydroxyapatite – Pullulan/dextran polysaccharide composite macroporous material for bone tissue engineering. Biomaterials 34, 2947–2959. https://doi.org/10.1016/j.biomaterials.2013.01.049

Furukawa, Y., Shimada, W., 1993. Three-dimensional pattern formation during growth of ice dendrites — its relation to universal law of dendritic growth. J. Cryst. Growth 128, 234–239. https://doi.org/10.1016/0022-0248(93)90325-Q

Geidobler, R., Winter, G., 2013. Controlled ice nucleation in the field of freeze-drying: Fundamentals and technology review. Eur. J. Pharm. Biopharm., SI: EJPB Freeze Drying (Invited only) 85, 214–222. https://doi.org/10.1016/j.ejpb.2013.04.014

Grenier, J., Duval, H., Barou, F., Lv, P., David, B., Letourneur, D., 2019. Mechanisms of pore formation in hydrogel scaffolds textured by freeze-drying. Acta Biomater. 94, 195–203. https://doi.org/10.1016/j.actbio.2019.05.070

Gripon, P., Rumin, S., Urban, S., Le Seyec, J., Glaise, D., Cannie, I., Guyomard, C., Lucas, J., Trepo, C., Guguen-Guillouzo, C., 2002. Infection of a human hepatoma cell line by hepatitis B virus. Proc. Natl. Acad. Sci. 99, 15655–15660. https://doi.org/10.1073/pnas.232137699

Guerrero, J., Catros, S., Derkaoui, S.-M., Lalande, C., Siadous, R., Bareille, R., Thébaud, N., Bordenave, L., Chassande, O., Le Visage, C., Letourneur, D., Amédée, J., 2013. Cell interactions between human progenitor-derived endothelial cells and human mesenchymal stem cells in a three-dimensional macroporous polysaccharide-based scaffold promote osteogenesis. Acta Biomater. 9, 8200–8213. https://doi.org/10.1016/j.actbio.2013.05.025

Holly, E.E., Venkataraman, S.K., Chambon, F., Henning Winter, H., 1988. Fourier transform mechanical spectroscopy of viscoelastic materials with transient structure. J. Non-Newton. Fluid Mech. 27, 17–26. https://doi.org/10.1016/0377-0257(88)80002-8

Horinaka, J., Okuda, A., Yasuda, R., Takigawa, T., 2012. Molecular weight between entanglements for linear d-glucans. Colloid Polym. Sci. 290, 1793–1797. https://doi.org/10.1007/s00396-012-2728-5

Kang, H.-W., Tabata, Y., Ikada, Y., 1999. Fabrication of porous gelatin sca!olds for tissue engineering. Biomaterials 20, 6. https://doi.org/10.1016/S0142-9612(99)00036-8

Klembt Andersen, L., Antoranz Contera, S., Justesen, J., Duch, M., Hansen, O., Chevallier, J., Foss, M., Pedersen, F., Besenbacher, F., 2005. Cell volume increase in murine MC3T3-E1 pre-osteoblasts attaching onto biocompatible Tantalum observed by magnetic AC mode Atomic Force Microscopy. Eur. Cell. Mater. 10, 61–69. https://doi.org/10.22203/eCM.v010a07

Konstantinidis, A.K., Kuu, W., Otten, L., Nail, S.L., Sever, R.R., 2011. Controlled nucleation in freeze-drying: Effects on pore size in the dried product layer, mass transfer resistance, and primary drying rate. J. Pharm. Sci. 100, 3453–3470. https://doi.org/10.1002/jps.22561

Koivunotko, E., Merivaara, A., Niemelä, A., Valkonen, S., Manninen, K., Mäkinen, H., Viljanen, M., Svedström, K., Diaz, A., Holler, M., Zini, J., Paasonen, L., Korhonen, O., Huotari, S., Koivuniemi, A., Yliperttula, M., 2021. Molecular Insights on Successful Reconstitution of Freeze-Dried Nanofibrillated Cellulose Hydrogel. ACS Appl. Bio Mater. 4, 7157−7167. https://doi.org/10.1021/acsabm.1c00739

Labour, M.-N., Le Guilcher, C., Aid-Launais, R., El Samad, N., Lanouar, S., Simon-Yarza, T., Letourneur, D., 2020. Development of 3D Hepatic Constructs Within Polysaccharide-Based Scaffolds with Tunable Properties. Int. J. Mol. Sci. 21, 3644. https://doi.org/10.3390/ijms21103644

Lack, S., Dulong, V., Le Cerf, D., Picton, L., Argillier, J.F., Muller, G., 2004. Hydrogels Based on Pullulan Crosslinked with sodium trimetaphosphate (STMP): Rheological study. Polym. Bull. 52, 429–436. https://doi.org/10.1007/s00289-004-0299-4

Lack, S., Dulong, V., Picton, L., Cerf, D.L., Condamine, E., 2007. High-resolution nuclear magnetic resonance spectroscopy studies of polysaccharides crosslinked by sodium trimetaphosphate: a proposal for the reaction mechanism. Carbohydr. Res. 342, 943–953. https://doi.org/10.1016/j.carres.2007.01.011

Lanouar, S., Aid-Launais, R., Oliveira, A., Bidault, L., Closs, B., Labour, M.-N., Letourneur, D., 2018. Effect of cross-linking on the physicochemical and in vitro properties of pullulan/dextran microbeads. J. Mater. Sci. Mater. Med. 29, 77. https://doi.org/10.1007/s10856-018-6085-x

Lavergne, M., Derkaoui, M., Delmau, C., Letourneur, D., Uzan, G., Le Visage, C., 2012. Porous Polysaccharide-Based Scaffolds for Human Endothelial Progenitor Cells. Macromol. Biosci. 12, 901–910. https://doi.org/10.1002/mabi.201100431

Le Visage, C., Letourneur, D., Chaubet, F., Autissier, A., 2015. Method for preparing porous scaffold for tissue engineering. US Patent 9,028,857.

Liu, S., Da, H., Hu, Y., Zhang, J., Chen, B., Zhang, H., Dong, X., Tong R., Li, Y., Zhou, W., 2020. Sodium alginate/collagen composite multiscale porous scaffolds containing poly(ε -caprolactone) microspheres fabricated based on additive manufacturing technology. RSC Adv. 10, 39241

Loh, Q.L., Choong, C., 2013. Three-Dimensional Scaffolds for Tissue Engineering Applications: Role of Porosity and Pore Size. Tissue Eng. Part B Rev. 19, 485–502. https://doi.org/10.1089/ten.teb.2012.0437

Nada, H., Furukawa, Y., 2005. Anisotropy in growth kinetics at interfaces between proton-disordered hexagonal ice and water: A molecular dynamics study using the six-site model of H2O, J. Cryst. Growth. 283, 242–256. doi:10.1016/j.jcrysgro.2005.05.057.

O'Brien, F.J., Harley, B.A., Yannas, I.V., Gibson, L., 2004. Influence of freezing rate on pore structure in freeze-dried collagen-GAG scaffolds. Biomaterials 25, 1077–1086. https://doi.org/10.1016/S0142-9612(03)00630-6

O'Brien, F.J., Harley, B.A., Yannas, I.V., Gibson, L.J., 2005. The effect of pore size on cell adhesion in collagen-GAG scaffolds. Biomaterials 26, 433–441. https://doi.org/10.1016/j.biomaterials.2004.02.052

Palmroth, A., Pitkänen, S., Hannula, M., Paakinaho, K., Hyttinen, J., Miettinen, S., Kellomäki, M., 2020. Evaluation of scaffold microstructure and comparison of cell seeding methods using micro-computed tomography-based tools. J. R. Soc. Interface 17, 20200102. https://doi.org/10.1098/rsif.2020.0102

Pawelec, K.M., Husmann, A., Best, S.M., Cameron, R.E., 2015. Altering crystal growth and annealing in ice-templated scaffolds. J. Mater. Sci. 50, 7537–7543. https://doi.org/10.1007/s10853-015-9343-z

Pawelec, K. M., Husmann, A., Best, S.M., Cameron, R.E., 2014a. Ice-templated structures for biomedical tissue repair: From physics to final scaffolds. Appl. Phys. Rev. 1, 021301. https://doi.org/10.1063/1.4871083

Pawelec, K M, Husmann, A., Best, S.M., Cameron, R.E., 2014. A design protocol for tailoring ice-templated scaffold structure. J R Soc Interface 11.

Pawelec, K. M., Husmann, A., Best, S.M., Cameron, R.E., 2014b. Understanding anisotropy and architecture in ice-templated biopolymer scaffolds. Mater. Sci. Eng. C Mater. Biol. Appl. 37, 141–147. https://doi.org/10.1016/j.msec.2014.01.009

Peppas, N.A., Merrill, E.W., 1977. Crosslinked poly(vinyl alcohol) hydrogels as swollen elastic networks. J. Appl. Polym. Sci. 21, 1763–1770. https://doi.org/10.1002/app.1977.070210704

Piazolo, S., Montagnat, M., Blackford, J.R., 2008. Sub-structure characterization of experimentally and naturally deformed ice using cryo-EBSD. J. Microsc. 230, 509–5019. https://doi.org/10.1111/j.1365-2818.2008.02014.x

Qian, L., Zhang, H., 2011. Controlled freezing and freeze drying: a versatile route for porous and micro-/nano-structured materials. J. Chem. Technol. Biotechnol. 86, 172–184. https://doi.org/10.1002/jctb.2495

Schneider, C.A., Rasband, W.S., Eliceiri, K.W, 2012. NIH Image to ImageJ: 25 years of image analysis. Nature Methods 9, 671-675. https://doi.org/10.1038/nmeth.2089

Scotti, K. L., Dunand, D. C., 2018. Freeze casting – A review of processing, microstructure and properties via the open data repository, FreezeCasting.net. Progress in Materials Science 94, 243–305. https://doi.org/10.1016/j.pmatsci.2018.01.001

Searles, J.A., Carpenter, J.F., Randolph, T.W., 2001. The ice nucleation temperature determines the primary drying rate of lyophilization for samples frozen on a temperature-controlled shelf. J. Pharm. Sci. 90, 12. https://doi.org/10.1002/jps.1039

Shao, G., Hanaor, D.A.H., Shen, X., Gurlo, A., 2020. Freeze Casting: From Low-Dimensional Building Blocks to Aligned Porous Structures—A Review of Novel Materials, Methods, and Applications. Adv. Mater. 32, 1907176. https://doi.org/10.1002/adma.201907176

Shepherd, J.H., Howard, D., Waller, A.K., Foster, H.R., Mueller, A., Moreau, T., Evans, A.L., Arumugam, M., Bouët Chalon, G., Vriend, E., Davidenko, N., Ghevaert, C., Best, S.M., Cameron, R.E., 2018. Structurally graduated collagen scaffolds applied to the ex vivo generation of platelets from human pluripotent stem cell-derived megakaryocytes: Enhancing production and purity. Biomaterials 182, 135–144. https://doi.org/10.1016/j.biomaterials.2018.08.019

Shibkov, A.A., Golovin, Yu.I., Zheltov, M.A., Korolev, A.A., Leonov, A.A., 2003. Morphology diagram of nonequilibrium patterns of ice crystals growing in supercooled water. Phys. Stat. Mech. Its Appl. 319, 65–79. https://doi.org/10.1016/S0378-4371(02)01517-0

Shibkov, A.A., Zheltov, M.A., Korolev, A.A., Kazakov, A.A., Leonov, A.A., 2005. Crossover from diffusion-limited to kinetics-limited growth of ice crystals. J. Cryst. Growth 285, 215–227. https://doi.org/10.1016/j.jcrysgro.2005.08.007

Tao, Y., Zhang, R., Xu, W., Bai, Z., Zhou, Y., Zhao, S., Xu, Y., Yu, D., 2016. Rheological behavior and microstructure of release-controlled hydrogels based on xanthan gum crosslinked with sodium trimetaphosphate. Food Hydrocoll. 52, 923–933. https://doi.org/10.1016/j.foodhyd.2015.09.006

Treloar, L.R.G., 1975. The physics of rubber elasticity, Third Edition. ed. Oxford University Press, Oxford, [Eng].

Vashist A., Ahmad, S., 2015. Hydrogels in Tissue Engineering: Scope and Applications. Current Pharmaceutical Biotechnology 16, 606-620.

Vali, G., 1994. Freezing Rate Due to Heterogeneous Nucleation. J. Atmospheric Sci. 51, 1843–1856. https://doi.org/10.1175/1520-0469(1994)051<1843:FRDTHN>2.0.CO;2

Van Vlierberghe, S., Dubruel, P., Schacht, E., 2011. Biopolymer-Based Hydrogels As Scaffolds for Tissue Engineering Applications: A Review. Biomacromolecules 12, 1387–1408. https://doi.org/10.1021/bm200083n

Zhang, H., 2018. Ice Templating and Freeze-Drying for Porous Materials and Their Applications. Wiley-VCH Verlag GmbH & Co. KGaA.

Zhang, H., Cooper, A.I., 2007. Aligned Porous Structures by Directional Freezing. Adv. Mater. 19, 1529–1533. https://doi.org/10.1002/adma.200700154